Earth Syst. Dynam. Discuss., 5, 473–528, 2014
www.earth-syst-dynam-discuss.net/5/473/2014/
doi:10.5194/esdd-5-473-2014

Earth System Dynamics
Discussions
Open Access

Burial-nutrient feedbacks amplify the sensitivity of carbon dioxide to changes in organic matter remineralisation

R. Roth[1,2], **S. P. Ritz**[1,2], **and F. Joos**[1,2]

[1]Climate and Environmental Physics, Physics Institute, University of Bern, Bern, Switzerland
[2]Oeschger Centre for Climate Change Research, University of Bern, Bern, Switzerland

Received: 28 March 2014 – Accepted: 4 April 2014 – Published: 14 April 2014

Correspondence to: R. Roth (roth@climate.unibe.ch)

Published by Copernicus Publications on behalf of the European Geosciences Union.

Abstract

Changes in the marine remineralization of particulate organic carbon (POC) and calcium carbonate potentially provide a positive feedback under climate change. The responses to changes in remineralization length scales are systematically mapped with the Bern3D ocean–sediment model for CO_2 and tracer fields for which observations and palaeoproxies exist. Spatio-temporal evolutions are captured by empirical orthogonal functions. Results show that the “sediment burial-nutrient feedback” amplifies the initial response in atmospheric CO_2 by a factor of four to seven. A temporary imbalance between the weathering flux and the burial of organic matter and calcium carbonate lead to sustained changes the ocean's phosphate and alkalinity inventory and in turn in surface nutrient availability, marine productivity, and atmospheric CO_2. It takes decades to centuries to reorganize tracers and fluxes within the ocean, many millennia to approach equilibrium for burial fluxes, while δ^{13}C signatures are still changing 200 000 years after the perturbation. CO_2 sensitivity is with 1.7 ppm m^{-1} about fifty times larger for a unit change in the remineralisation depth of POC than of calcium carbonate. The results highlight the role of organic matter burial for atmospheric CO_2 and the substantial impacts of seemingly small changes in POC remineralisation.

1 Introduction

The mixing ratio of CO_2 in the atmosphere varied by ~ 80–100 parts per million (ppm) in past glacial–interglacial cycles on timescales of ~ 100 thousand years (kyr) (Petit et al., 1999; Siegenthaler et al., 2005; Lüthi et al., 2008). Biogeochemical processes leading to their variations are still poorly quantified (Sigman and Boyle, 2000; Archer et al., 2000; Sigman et al., 2010; Fischer et al., 2010), especially the slowly acting mechanisms. The tight coupling between atmospheric CO_2 and temperature calls for temperature-mediated feedbacks in the global carbon cycle. Several hypothesis have been discussed to explain the CO_2 drawdown during the Last Glacial

Maximum (LGM), these include: ocean circulation and stratification changes (Watson and Garabato, 2006; Bouttes et al., 2010; Völker and Köhler, 2013), continental weathering (Munhoven, 2002), volcanism (Huybers and Langmuir, 2009; Roth and Joos, 2012), changes in the ocean's biological pump, e.g. by changes in its strength as modulated by the availability of micro- and macro-nutrients (Parekh et al., 2008; Tschumi et al., 2011; Oka et al., 2011) or changes in the export rain ratio (Matsumoto et al., 2007; Tschumi et al., 2011).

Changes in the remineralisation of particulate organic matter (POM) has recently been suggested as a further feedback which may considerably contribute to past and future CO_2 changes. How POM is converted to inorganic nutrients in the water column depends on the speed with which the particles sink towards the ocean floor and on the local rate of remineralisation. An increase in temperature is expected to promote bacterial activities and to increase local remineralisation rate (Bendtsen et al., 2002), and to increase viscosity and thus the speed of sinking particles (Taucher et al., 2014). In addition, changes in ecosystem structure in the surface ocean potentially affect the size and density distribution of the settling particles and thus sinking speed (Armstrong et al., 2002, 2009). In short, such changes in the organic matter cycle influence the surface-to-deep transport of nutrients and carbon and thus increase respired carbon storage in the deep ocean. As a result, a deepening of the remineralisation depth of POM – corresponding to a lower rate of degradation as e.g. induced by a lower bacterial activity – results in a drawdown of atmospheric CO_2. This mechanisms has been discussed in several studies: Matsumoto (2007) estimated a CO_2 drawdown of ~ 35 ppm for a 5 °C ocean cooling experiment and using a 3-D ocean model. On the other hand, Chikamoto et al. (2012) finds only a small CO_2 sensitivity to a 5 °C ocean cooling (–9 ppm). Kwon et al. (2009) suggest a CO_2 drawdown by 10–27 ppm for an increase in the e-folding depth of POM remineralisation of 24 m. Recently, Segschneider and Bendtsen (2013) estimated a reduction of anthropogenic CO_2 uptake rates of 0.2 gigatons of carbon (GtC) per year by 2100 AD in future emission scenarios. Taucher et al. (2014) isolate the influence of viscosity changes in a global warming simulation and found that ocean carbon uptake is 17 % higher when considering temperature-driven viscosity changes on particle sinking speed compared to a control. As a caveat, all these studies neglect ocean–sediment interactions and the weathering-burial cycle.

Ocean–sediment interactions (including weathering-burial) can amplify or mitigate a perturbation in the ocean–atmosphere system. For example, excess anthropogenic carbon is ultimately removed from the ocean–atmosphere system by ocean sediment buffering and burial. On the other hand, the change in atmospheric CO_2 in response to a change in calcite export is about four times larger in an "open" system considering sediment interactions as compared to a "closed" ocean–atmosphere system (e.g. Tschumi et al., 2011). Tschumi et al. (2011) identified the importance of the nutrient-burial feedback for a range of mechanisms with the potential to explain low glacial CO_2. They conclude that the long-term balance between burial of organic material and tracer input into the ocean through weathering, typically neglected in earlier studies, must be considered when investigating the glacial–interglacial evolution of atmospheric CO_2 and related tracers.

As the mean remineralisation depth of POM is altered, the deposition of POM on the seafloor and burial rates are also expected to change. This leads to a transient imbalance between burial and continental weathering fluxes on multi-millennial time scales. These consequences have not been discussed so far in a systematic manner and in the context of a 3-dimensional, dynamic model. Matsumoto et al. (2007) discuss the effect of altered temperature on export and remineralisation rate. They applied an ecosystem model embedded in a dynamic ocean model and simulate a change in the export rain ratio between particulate organic carbon and $CaCO_3$ in response to altered temperatures. They argue that the effect of temperature on POC degradation has a more dominant impact on the export rain ratio than on POC remineralisation depth scale. Accordingly, only the change in rain ratio is prescribed in a box-type ocean–sediment model to estimate changes in atmospheric CO_2, but the impact of a deepening of the remineralisation depth as well as changes in the burial of organic matter are neglected by Matsumoto and colleagues. Menviel et al. (2012) showed in transient model simulations over the last glacial cycle with the Bern3D model that a temperature-dependent remineralisation rate may contribute to the reconstructed CO_2 variations.

The goals of this study are to systematically map the spatio-temporal response to alterations in the remineralisation depth in a 3-dimensional, dynamic model setting. The response in carbon isotopes, nutrients and other palaeo proxies as well as in in atmospheric CO_2 and its carbon isotopic signature are analyzed. Results are also characterised in terms of empirical orthogonal functions (EOFs) that may be used to build cost-efficient substitute models. A series of well-defined sensitivity experiments is performed, where the POM remineralisation depth is changed in a step-like manner. The Bern3D dynamic ocean model of intermediate complexity is applied with prognostic formulations of export production coupled to a 3-D sediment component, allowing for the quantification of the long-term sediment feedback associated with both POM and $CaCO_3$ burial on marine chemistry and atmospheric CO_2 and $^{13}CO_2$. In addition, changes in the calcite redissolution rate are considered. We show that previous estimates of the sensitivity of POM remineralisation rate changes strongly underestimate the long-term feedback on a multi-millennial timescale, pointing to a potential importance of this mechanism to explain low-frequency CO_2 and $^{13}CO_2$ variations. The nutrient-burial feedback (Tschumi et al., 2011) amplifies the initial response to a deepening of the POM remineralisation by a factor between three and seven in our model.

2 Model

2.1 Physical model

We invoke an updated (see Appendix) version of the Bern3D Earth-System model of intermediate complexity (EMIC). Its frictional-geostrophic balance 3-D ocean component is based on the model of Edwards and Marsh (2005) and as further improved as described in Müller et al. (2006). It includes an isopycnal diffusion scheme and

Gent–McWilliams parameterisation for eddy-induced transport (Griffies, 1998). The horizontal resolution is now set to 41 × 40 grid boxes in the horizontal, while 32 logarithmically spaced layers in the vertical are used. Wind stress is prescribed according to the monthly climatology from NCEP/NCAR (Kalnay et al., 1996). The atmosphere is represented by a 2-D energy and moisture balance model (EBM) with the same horizontal resolution as the ocean as described in Ritz et al. (2011a). Following Weaver et al. (2001), outgoing longwave radiative fluxes are parameterised after Thompson and Warren (1982) with additional radiative forcings due to e.g. CO_2, other greenhouse gases and volcanic aerosols. The sea ice model component is based on work by Semtner (1976) and Hibler (1979) and is similar to the sea ice model of Edwards and Marsh (2005).

Air-sea gas exchange for CO_2 and $^{14}CO_2$ is implemented according to the OCMIP-2 protocol (Orr and Najjar, 1999; Najjar et al., 1999), but with a reduced scaling factor (Müller et al., 2008). $^{14}CO_2$ is not fractionated during air–sea gas exchange while $^{13}CO_2$ is fractionated as a function of temperature and carbonate chemistry as detailed in Müller et al. (2008).

2.2 The marine biogeochemical cycle and particle remineralisation

The marine biogeochemical module computes the cycling of carbon (C), alkalinity (Alk), phosphate (PO_4), iron (Fe), oxygen (O_2), silica (SiO_2), and of the carbon isotopes ^{13}C and ^{14}C. Carbon is represented as dissolved inorganic carbon (DIC) and labile dissolved organic carbon (DOC).

Prognostic formulations link marine productivity and dissolved organic matter (DOM) to available nutrients (PO_4, Fe, SiO_2), temperature, sea ice and light using Michaelis–Menten limiting terms (Doney et al., 2006) in the euphotic zone (uppermost 75 m) described in Parekh et al. (2008) and Tschumi et al. (2011). POM is exported from the euphotic zone as a constant fraction (σ) of new production (Γ_{new}) at the reference depth z_0. The remainder (i.e. $1 - \sigma$) is transferred to the labile DOM pool. The export between

$CaCO_3$ and particulate organic carbon (POC) – i.e. the export “rain ratio” – is constant (~ 0.075) unless silicic acid is abundant; in this case diatom growth is favored at the expense of calcifer growth. The rain ratio is therefore lowered in these SiO_2 replete regions, which is primarily the case in the Southern Ocean upwelling regions (south of $\sim 60^\circ$ S) (Fig. 1).

The carbon isotope fractionation factor, $\alpha_{[CO_2]-C_{org}}$, between dissolved CO_2 and organic carbon depends on the concentration of dissolved CO_2 ($[CO_2]$) in units of µmol kg^{-1}, according to (Freeman and Hayes, 1992):

$$\alpha_{CO_2-C_{org}} = \frac{^{13}R([CO_2])}{^{13}R(C_{org})} = 1.00119 + 0.01203 \cdot \log[CO_2]. \qquad (1)$$

This results in an isotopic signature of POC around −20 ‰. Important in our context (see Sect. 3.1.3), a lowering of $[CO_2]$, or correspondingly of pCO_2, by 10 % yields a change in the isotopic signature of POC by +0.55 ‰.

DOM remineralisation is implemented using a fixed decay time of 0.5 yr. The remineralisation of sinking POM results from the prescribed depth-dependent scaling of the flux of particulate organic phosphorus (POP) and POM (Fig. 2), known as the “Martin curve” (Martin et al., 1987):

$$F_{POP}(z) = F_{POP}(z_0) \cdot \left(\frac{z}{z_0}\right)^{-\alpha} \quad \text{for} : z > z_0. \qquad (2)$$

Here, $F_{POP}(z)$ is the downward flux POP at depth z (z positive downwards) and $F_{POP}(z_0)$ the POP flux at the reference depth $z_0 = 75$ m. Other elements such as carbon, carbon isotopes, oxygen and alkalinity are coupled to POP and DOP by constant elemental (Redfield) ratios set to $P : C : Alk : O_2 = 1 : 117 : -17 : -170$. The exponent α defines the shape of the curve: a high value of α shoals while a low α deepens the depth at which organic matter is remineralised. α is set to a globally uniform value of 0.83 in the standard setup.

The empirical relationship of Eq. (1) – a result of a fit through sediment-trap data – makes per se no statement on the *rate* of remineralisation as both sinking speed and degradation contribute to the vertical profile of observed POM concentrations. The remineralisation of POP, R, can be written as:

$$R(z) = k \cdot [\mathrm{POP}] = k/\bar{v} \cdot F_{\mathrm{POP}}(z) = \mathrm{d}F(z)/\mathrm{d}z. \qquad (3)$$

k is the remineralisation rate coefficient in s^{-1}, [POP] the concentration of POP in the water, $\bar{v}$ the mean sinking speed of POP. It follows, by rearranging Eq. (3) and with the help of Eq. (2), for the apparent rate of remineralisation, k_{app} (in units of m^{-1}):

$$k_{\mathrm{app}} = k/\bar{v} = \frac{1}{F_{\mathrm{POP}}(z)} \cdot \mathrm{d}F_{\mathrm{POP}}(z)/\mathrm{d}z = -\alpha \left(\frac{z_0}{z}\right)^{-1}. \qquad (4)$$

The apparent remineralisation rate ($k/\bar{v}$) decreases inversely proportional with depth z (Fig. 2b). Although the POM degradation rate is not constant over depth, we define an e-folding depth (l_{POM}) for convenience. That is, the depth at which the downward POM flux has diminished to $1/e \approx 37\,\%$:

$$F_{\mathrm{POP}}(z = l_{\mathrm{POM}})/F_{\mathrm{POP}}(z_0) = (1/e) \rightarrow l_{\mathrm{POM}} = z_0 \cdot e^{1/\alpha}. \qquad (5)$$

l_{POM} is 250 m for the standard value of $\alpha = 0.83$. The flux of organic matter is sketched in Fig. 2. The downward flux of calcite (F_{calc}) decreases exponentially with depth with a lengthscale l_{calc}:

$$F_{\mathrm{calc}}(z) = F_{\mathrm{calc}}(z_0) \cdot e^{-\frac{z - z_0}{l_{\mathrm{calc}}}} \quad \text{for} : z > z_0. \qquad (6)$$

A 10-layer sediment diagenesis model (Heinze et al., 1999; Gehlen et al., 2006) is coupled at the ocean floor. It features the same horizontal resolution as the ocean model. It dynamically calculates the advection, remineralisation/redissolution and bioturbation of solid material ($\mathrm{CaCO_3}$, POM, opal and clay) within the top 10 cm of the seafloor as well as pore-water chemistry and diffusion as described in detail in Tschumi et al. (2011). The model assumes conservation of volume, i.e. the entire column of the sediments is pushed downwards if deposition exceeds redissolution into pore waters. The POM redissolution is primarily a function of local oxygen levels while the local CO_3^{2-} concentration determines whether, and at which rate, $CaCO_3$ dissolves. The latter mechanism is crucial for simulating the so-called carbonate compensation. The weathering fluxes of DIC, Alk, PO_4 and SiO_2 are prescribed along the coastal surface ocean. This representation of ocean–sediment interactions implies that the model is "open" concerning the cycling of carbon and nutrients. Ocean–atmosphere tracer inventories are not conservative quantities anymore as transient imbalances of the weathering and burial fluxes may increase or decrease the total tracer inventories in the model. In this manuscript, the term "burial" refers to the net tracer-flux at the ocean–sediment interface, i.e. *deposition–redissolution* of the particulate material. Using this definition, changes in the atmosphere–ocean tracer inventory are directly linked to changes in the burial fluxes. Note that this flux can transiently differ from the mass-flux into the consolidated sediment layer (i.e. below 10 cm in the model), as the sediment diagenesis layer acts as a buffer.

Here, no land biosphere module is coupled to the Bern3D as our interest is on the ocean–atmosphere response to changes in the remineralisation profile of POM and calcite.

2.3 Model initialisation and preindustrial state

The model is spun up over 60 000 years to a preindustrial equilibrium corresponding to 1765 AD boundary conditions. CO_2 is prescribed to 278 ppm and $\delta^{13}C$ of CO_2 to -6.3 ‰. This results in a oceanic DIC inventory of $\sim$37 400 GtC, similar to the 37 510 GtC as estimated from the GLODAP (Key et al., 2004) and World Ocean Atlas (Locarnini et al., 2010; Antonov et al., 2010) datasets. The loss of tracer due to burial of particulate matter is compensated during the spin up by a variable weathering as to conserve oceanic inventories of tracers. After the system equilibrated, the weathering fluxes are kept constant at the rate diagnosed during the end of the spin up. Global integrated fluxes of POM export, deposition and burial are 11.7, 0.63 and 0.18 $\mathrm{Gt\,C\,yr^{-1}}$ for preindustrial conditions. Table 1 provides an overview on steady-state export, deposition, burial fluxes of POM, calcite and opal and of the weathering/burial fluxes of different tracers. The model is able to represent the observation-based distribution of tracers in the ocean interior (Appendix, Fig. A1). Known shortcomings are a too sluggish formation of Antarctic Bottom Water in the Atlantic and intermediate waters do not penetrate far enough towards the equator.

Modelled POM and calcite export (Fig. 1a and b) is low in the subtropical gyres as well as in the Arctic and around Antarctica. Generally high export fluxes are found in upwelling regions off Africa and South America, in the northern North Pacific and Atlantic and in the Southern Ocean between ~ 40° S and 60° S. The pattern is comparable to those simulated by state-of-the-art Earth System models (ESM) and to observation-based estimates (Schneider et al., 2008; Steinacher et al., 2010). Similarly as in ESMs, there is too much new production in the eastern part of the tropical Indian and too little in the Arabian Sea. Modelled opal export (Fig. 1c) features the well-known belt along 60° S and maxima in the tropical East Pacific and the northwest Pacific.

2.4 Experiments

Sensitivity experiments are performed where l_{POM} (or equivalently α) and/or l_{calc} are changed in a step-wise manner (Fig. 3a). The model is then re-equilibrated for up to 200 kyr (some experiments are only integrated for 50 and 100 kyr, respectively) in a prognostic mode where atmospheric $\mathrm{CO_2}$ and $\delta^{13}\mathrm{C}$ evolve freely. As weathering fluxes are kept constant in the perturbation experiments, global inventories of tracers in the atmosphere–ocean–sediment system are not conserved (Fig. 3h and i). We refer to this setup as “open system”. We also run the system in an atmosphere–ocean only setup referred-to as “closed system”. This setup is very similar to the model invoked by e.g. Kwon et al. (2009). The difference in results between the open and closed system is the contribution by the sediment and weathering-burial feedbacks.

We performed a range of sensitivity experiments where l_{POM} is varied between 225 and 375 m. We will discuss as an illustrative example results from experiments where the exponent α is changed from 0.83 to 0.77, corresponding to a change in l_{POM} from 250 to 275 m.

We restrict our analysis to changes in α (and thus l_{POM}) as the link to temperature changes seems non-trivial. Changes in ecosystem structure in the euphotic zone and corresponding changes in the quality and sinking speed of POM have the potential to influence remineralisation rates in addition to changes in bacterial activities in the twilight zone and the deep ocean. For illustrative purposes, we may describe a potential relation between temperature changes in the water column and changes in α. Let us assume a spatially uniform temperature change, a constant mean particle settling velocity and that the remineralisation rate of POM is temperature driven and can be described by $k_{\mathrm{app}}(T) = k_{\mathrm{app}}(T_0) \cdot Q_{10}^{(T-T_0)/10^\circ\mathrm{C}}$. With the help of Eq. (2), a change in α from $\alpha_0 = 0.83$ to $\alpha_1 = 0.77$ translates for a Q_{10} value of 2 to a mean change in temperature $\Delta T = 10^\circ\mathrm{C}\ln(\frac{\alpha_1}{\alpha_0})/\ln(Q_{10}) = -1.1\,^\circ\mathrm{C}$.

Changing concentrations of atmospheric CO_2 as induces by biological changes are not fed back to the radiative code in the standard setup as this so-called oceanic climate-carbon feedback has been systematically analyzed elsewhere (Arora et al., 2013; Plattner et al., 2008; Joos et al., 1999). This implies that the physical part of the model (e.g. ocean circulation) remains unchanged during the experiments.

2.5 An impulse response – empirical orthogonal function representation

The remineralisation depth is changed in a step-wise manner in our experiments. The underlying rational is that the response of a linear system is fully characterised by its response, r, to a pulse-like perturbation or to a step change in forcing, Δf. The change in variable V at time t and location $\boldsymbol{x}$ to any evolution of a unique forcing f is given by:

$$\Delta V(\boldsymbol{x},t) = \int_{-\infty}^{t} \Delta f(t') \times r(\boldsymbol{x},t-t')\mathrm{d}t'. \tag{7}$$

For example, the variable may be the ^{13}C signature of dissolved inorganic carbon as recorded by a sediment core at location $\boldsymbol{x}$ and the forcing may be a characteristic change in the POM remineralisation depth. We note that the carbon cycle is non-linear and above equation is only an approximation for sufficiently small changes in f to remain within the quasi-linear range of the system.

The response r describe the response to a forcing in space and time and represents thus a large matrix of the dimension (number of grid cells) × (number of time steps). It may be convenient to reduce the dimensionality of r by applying an empirical orthogonal function (EOF) analysis. Here, r is represented as the superposition of a set of mutually orthogonal spatial patterns, EOF_i, and the time-dependent scalar coefficients termed principal components, PC_i:

$$r(\boldsymbol{x},t) = \sum_i \mathrm{PC}_i(t) \cdot \mathrm{EOF}_i(\boldsymbol{x}). \tag{8}$$

Each of the PC-EOF pairs i is computed from the model output in successive order to explain the maximum possible variance in r. Often, it is sufficient to consider the first few PC-EOF pairs only to capture most of the variance in a field. In addition, PC_i may be fitted by analytical functions. Then, r is represented by two to three analytical functions and two to three spatial fields – a great ease in data handling. Equations (7) and (8) may be combined to build a cost-efficient Green's function substitute model (Joos et al., 1996; Hooss et al., 2001).

3 Results

3.1 l_{POM} changes

3.1.1 Ocean response

We start discussion by analyzing changes in fluxes and tracer distributions for an increase of l_{POM} by 25 m from 250 to 275 m. This results in a decrease in the fraction of the POM export that is remineralised above ~250 m and in an increase below (Fig. 2c). These changes affect tracer distributions in the model and in turn surface nutrient availability, productivity, export, deposition, and burial fluxes of POM and calcite (Fig. 3). Both in the open and closed system, the remineralisation of POM at deeper depths leads to a larger surface-to-deep ocean gradient in nutrients, to less nutrients in subsurface water and to less nutrient input into the euphotic zone. As a result, surface water concentrations of PO_4 decreases leading to a decrease in global export production of POM and $CaCO_3$ by ~ 12 % (Fig. 3b and c).

The step-wise change in remineralisation depth leads to an initial spike in POM deposition. Then deposition is decreasing in parallel with export, but remains above the initial deposition rate throughout the simulation. The higher deposition leads to a temporary excess of POM burial compared to the closed system (or the weathering input) (Fig. 3f and h; P and C fluxes scale with the Redfield ratio of 1 : 117) and consequently to a decrease in the ocean inventory of phosphate further reducing organic matter production in the euphotic zone. The decrease in POM and calcite exports occurs in two phases. First, the deepening of the remineralisation depth leads to a redistribution of nutrients within the ocean on multi-decadal to century scale. Second, whole ocean phosphate inventory and particle export slowly decrease on millennial time scale to reach a new equilibrium when the balance between burial and weathering input of phosphorus is reestablished around 40 to 50 kyr after the step change (Fig. 3f, dashed line).

Next, we discuss the processes and the time-evolution of POM and calcite burial, here taken as the flux leaving the ocean at the sediment interface. Increased POM deposition tends to increase POM burial. In addition, reduced oxygen concentrations in the sediment pore water, e.g. as a result of an oxygen reduction in the deep ocean, tend to transiently decrease redissolution (the fraction of POC oxidised decreases), further promoting POM removal from the system. Finally, the equilibrium POM burial rate has to balance input of phosphorus by weathering. The result is an initial spike in POC burial by almost 80 %, about four times larger than the relative initial increase in deposition. Afterwards, POC burial decreases quickly within a few centuries and then more slowly to approach steady state over the next few millennia.

Similarly, the temporal evolution of calcite burial is driven by changes in deposition and redissolution fluxes. Calcite deposition decreases according to the global decrease in primary production and export. As the lysocline shoals as a consequence of the disturbed seawater chemistry – CO_3^{2-} initially decreases in the deep ocean – more sediments are exposed to undersaturated waters, leading to an increased redissolution flux for the first ∼ 5 kyr. Thereafter, the lysocline starts to deepen until burial matches weathering input; in the long run, the lysocline deepens by ∼ 800 m in the Pacific. The result is an initial drop in calcite burial by about 10 % and a very slow recovery to the initial burial rate over the next 100 kyr. The imbalance in the burial and weathering fluxes of POM and calcite causes a removal of only 4.2×10^{14} mol of carbon (5 Gt C) from the ocean and the addition of about 55×10^{15} equivalent of alkalinity (a mean Alk increase of ∼ 39 μmol L^{-1}) (Fig. 3h and i). The reduced loss of carbon by calcite burial is largely offset by the enhanced burial of POM, while both a reduced calcite burial and an enhanced POM burial tend to increase ocean alkalinity. Overall, the ocean inventory in DIC is also increased as the ocean absorbs about 70 Gt C from the atmosphere (see next section). The whole ocean phosphorus inventory is affected by the excess POP burial and decreases by 2.2×10^{14} mol P.

The adjustment to a new equilibrium takes longer for the phosphorus inventory, co-governing POM burial than for the alkalinity inventory, co-governing calcite burial.

63 % of the final perturbation in the phosphorus and alkalinity inventory is reached after 8.5 kyr (Fig. 3f) and after 32 kyr (Fig. 3f), respectively. The difference in time scales is linked to the difference in mean residence time of 23 kyr for phosphorus (3030 T mol/0.13 T mol yr^{-1}) and of 253 kyr for alkalinity (3290 P eq/0.013 P eq yr^{-1}).

Regional changes in the surface concentration of PO_4, POM export and POM deposition are distinct (Fig. 4). After 50 kyr PO_4 is reduced almost everywhere in the surface ocean. Smallest changes are found in the oligothrophic regions where PO_4 is already strongly depleted in the control simulation. Relatively large reductions in the Southern Ocean and in the upwelling areas off South America and Africa are simulated. These are linked to the upwelling of less PO_4 rich waters as caused by the reduction in the total phosphate inventory of the ocean by excess POP burial. Relatively large reductions are also simulated in the subtropical gyres in the Pacific and Atlantic as well as in the eastern Indian where the model features too high PO_4 concentrations in the standard setup.

POM export (Fig. 4b) is hardly reduced in the Southern Ocean while substantial reductions are simulated in equatorial regions and in the northern North Pacific and North Atlantic. POM deposition increases along the productivity belt in the Southern Ocean and in the upwelling region off South America and Africa and in the northwestern North Pacific. There is also an increase in POM deposition in the eastern tropical Indian ocean, which is linked to too excessive productivity in this area. In the North Atlantic, the influences of the reduction in POM export and the increase in remineralisation depth on POM deposition nearly cancel.

Next, we discuss the redistribution of tracers within the ocean for the new equilibrium in the closed and open system. The distribution changes in the closed system are occurring in the first two millennia while it takes many millennia to approach the equilibrium in the open system. Figure 5 shows the resulting equilibrium anomalies w.r.t. the control simulation for PO_4, DIC, CO_3^{2-} and oxygen in a transect through the Atlantic, Southern Ocean and Pacific (the transect is highlighted in red in Fig. A2b).

In the closed system (i.e. without sediment module) the ocean's PO_4 inventory is conserved and a deepening of the remineralisation depth leads to a depletion in PO_4 in the upper ocean and an increase in the deep. The pattern reflects the major transport pathways in the ocean showing reduced PO_4 concentration in North Atlantic Deep Water and enhanced concentration in Antarctic Bottom Water in the Atlantic and Pacific. As expected, this pattern is mirrored in subsurface waters by DIC, oxygen and $\delta^{13}C$ as these tracers are linked to PO_4 by constant Redfield elemental ratios in biological fluxes. At the same time, CO_3^{2-} (and Alk) is slightly increased in the upper part of the water column as less POM is remineralised in the upper ocean (POM remineralisation consumes Alk). CO_3^{2-} (and Alk) is lowered in the deep as less calcite and more POM is remineralised.

In the setup with sediment model, downward fluxes of POM (and $CaCO_3$) are not remineralised at the seafloor, but deposited on the model's sediment layer and undergo bioturbation, remineralisation and vertical transport. The ocean inventory of PO_4, and Alk change substantially in response to excess POM and reduced calcite burial as discussed above. As a results, PO_4 is reduced and Alk increased in the entire ocean compared to the control. The changes in DIC are more subtle and regionally distinct. Reduced remineralisation in the thermocline leads to negative anomalies in the Atlantic and Pacific. The increase in Alk causes a change in the partitioning between dissolved CO_2, bicarbonate, and carbonate ion. The results is a decrease in pCO_2, an increase in carbonate ion, and an increase in DIC in the surface ocean. This positive DIC anomalies are communicated to the deep in the North Atlantic and Southern Ocean, where the positive DIC anomalies in the Southern Ocean and the deepest layers of the Pacific and Atlantic ocean are partly maintained.

We apply principal component analysis on the spatio-temporal anomaly-patterns of the open-system response. Generally we find that most of the full-model variance can be sufficiently described by 2 empirical orthogonal functions (EOFs). Figure 6 shows the two dominant EOFs and corresponding timeseries for CO_3^{2-} anomalies. The resulting patterns strongly resemble those shown with Fig. 5g and h, i.e. the open- and closed-system response, namely (i) a slowly accumulating whole-ocean increase due to weathering-burial imbalance (ii) a tilt on the depth-gradient induced by the change in the biological pumps.

3.1.2 Response in atmospheric CO_2

We have shown that changes of l_{POM} lead to a much stronger perturbation in the ocean's carbonate system in an open model driven by the sustained imbalance between weathering and burial rates of DIC and Alk. The resulting whole-ocean increase in CO_3^{2-} leads to a decrease in seawater pCO_2 at the surface.

How does this influence the atmospheric CO_2 concentrations? In Fig. 7a, timeseries of the initial 50 kyr response are shown for both the closed (black) and open system (red). The magnitude of changes in atmospheric CO_2 is ~ 5 times higher in the setup with sediments compared to the setup without sediments at year 50 000. Atmospheric CO_2 decreased by 33.4 ppm in the open system and by 8.1 ppm in the closed system for a change in l_{POM} from 250 to 275 m. The CO_2 decrease is more than 100 ppm for a change in l_{POM} to 375 m. Atmospheric CO_2 is stabilised after ~ 2 kyr in the closed system, while at the same time the response in the open system is only ~ 40 % of the equilibrium response. 62 % of the equilibrium CO_2 change are reached after ~ 10 kyr and 93 % after ~ 50 kyr. The effective e-folding timescale, defined as the time when 63 % of the final anomaly is reached, is ~ 10 kyr in the open system and only 0.5 kyr in the closed system.

Global export production decreases in the standard experiment. We set up a sensitivity experiment to disentangle the influence of the reduced export flux vs. the change in the remineralisation profile. The export production climatology from the control run is prescribed in these perturbation experiments. As to be expected, changes in CO_2 increase by a factor of ~ 2–4 w.r.t. to the standard setup with prognostic production (see Fig. 7b). The constant export flux leads to a constant drain of nutrients and carbon from the ocean as burial fluxes continuously exceed weathering fluxes in the open system. In turn, the oceanic inventories slowly drift towards zero and negative values.

Therefore, no equilibrium-changes in CO_2 can be stated for the open system (Fig. 7b, shows anomalies after 50 kyr).

Next, we assess the sensitivity of atmospheric CO_2 to l_{POM} changes in different oceanic regions (Table 2). l_{POM} is changed in 3 latitudinal bands separately, namely 90–30° N, 30° N–30° S and 30–90° S. The sum of the CO_2 changes for the three regional experiments is with 35.6 ppm only slightly larger than for the global experiment (33.4 ppm). The tropical band covers the largest sea surface area (52 %) and most of the global POM export flux (~ 55 %). For a change of l_{POM} from 250 to 275 m, the tropical band alone contributes ~ 60 % of the CO_2 change. The effectiveness of l_{POM} changes per unit area or per unit POM export to reduce CO_2 is different for different regions (Table 2). Normalised sensitivities are highest in the northern extratropical band, likely linked to an efficient propagation of anomalies by North Atlantic Deep Water.

3.1.3 Carbon isotopes

Next, we further discuss the response in $\delta^{13}C$ of DIC and of atmospheric CO_2. $\delta^{13}C$ of atmospheric CO_2 is closely coupled through air–sea exchange to $\delta^{13}C$ of DIC in the surface ocean. We start with the closed system response. The spatio-temporal response in $\delta^{13}C$ of DIC mirrors that of PO_4 as the marine biogeochemical cycles of P and C and ^{13}C are coupled. The deepening of l_{POM} leads to less remineralisation of isotopically light (~ –20 ‰) POM in the upper ocean and more remineralisation in the deep. In turn $\delta^{13}C$ of DIC in the deep ocean decreases and $\delta^{13}C$ at depths shallower than ~ 1000 m increases (Fig. 8d). In addition, the decrease in surface water concentration of CO_2 leads to slightly less negative values of the fractionation factor for photosynthesis and thus for the transformation of inorganic carbon to POC; this tends to slightly decrease $\delta^{13}C$ in the surface ocean. The result is an increase in surface ocean and atmospheric $\delta^{13}CO_2$ by ~ 0.03 ‰ within 2 kyr (Fig. 8a and d).

Additional processes are important for the evolution of $\delta^{13}C$ of DIC and of CO_2 in the open system. (i) The excess burial of isotopically light POC during the first

~ 50 kyr tends to increase the average δ^{13}C signature in the ocean–atmosphere system. (ii) Similarly, burial of isotopically enriched calcite is reduced (relative to initial conditions and the weathering flux) during the first ~ 100 kyr; this tends to increase δ^{13}C during this period. (iii) The reduction in surface CO_2 is with 33 ppm about 4 times larger in the open system than in the closed system for an increase of l_{POM} to 275 m. This results in a less negative fractionation factor for POM formation (Freeman and Hayes, 1992) and tends to decrease δ^{13}C in the surface. (iv) At the new equilibrium, the input of ^{13}C by weathering must balance the loss of ^{13}C by burial as is the case for the flux of POC and calcite (Fig. 9). The consequence is that the positive shift in the POC fractionation factor leads to a loss of ^{13}C from the ocean until it is checked by a corresponding negative anomaly in ^{13}C of DIC in surface waters communicated to the POC and calcite burial fluxes.

In the surface ocean and the atmosphere, δ^{13}C is increasing during roughly the first 10–15 kyr by 0.08 ‰ in response to the closed system processes and in response to the anomalies in POC and calcite burial. Then, δ^{13}C decreases and the anomalies in δ^{13}C turn negative around 50 kyr followed by a further decrease until the end of the simulation in response to (iii) and (iv). The fractionation factor (expressed here as $\epsilon = 1000 \cdot (\alpha - 1)$) for photosynthesis (POC formation) changes roughly in parallel with surface ocean and atmospheric CO_2. It increases by 0.8 ‰ from −13.2 to 12.4 ‰ in the global average during the first ~ 100 kyr in the simulation where l_{POM} equals 275 m (Fig. 9a). In turn, the δ^{13}C signature of the POM burial flux increases by about 0.55 ‰ and starts to decreases only after about 50 kyr (Fig. 9b). δ^{13}C of the burial flux of calcite closely follows the evolution of δ^{13}C in the surface–atmosphere system. The whole-ocean's ^{13}C inventory is driven by changes in the δ^{13}C burial flux, expressed as the burial flux of C times its isotopic signature in ‰. The ^{13}C burial (Fig. 9c and d) is thus a convolution of the total C-burial, the particle's δ^{13}C and the POC-to-calcite ratio in the burial flux. The new equilibrium with zero δ^{13}C anomaly in the total burial flux is only achieved after the end of the simulation (200 kyr) (Fig. 9d). At the end of the simulation, the whole-ocean ^{13}C of DIC (and DOC) is still relaxing from its initial perturbation and a stabilisation is expected to take another 200 kyr or so. These long response-timescales are a result of the convolution of multiple slow processes and weak negative (stabilizing) feedbacks.

The effect on the radioactive carbon isotope ^{14}C is small compared to past natural variations. Δ^{14}C of atmospheric CO_2 increases by ~ 12 ‰ (~ 3 ‰ in the closed system). A constant rate of atmospheric ^{14}C production is applied. The increase can be attributed to the lower atmospheric CO_2 concentration, or more general, to the lower carbon inventory in the (open) system. The biologically mediated fluxes of ^{14}C within the ocean are small compared to the fluxes driven by advection, convection, and mixing. This explains the small sensitivity of Δ^{14}C to changes in the marine biological cycle.

3.2 l_{calc} changes

It has been suggested that changes in the rate of $CaCO_3$ dissolution in the upper ocean will be a significant feedback affecting atmospheric CO_2 concentrations and future climatic changes (e.g. Barrett et al., 2014). To this end, we prescribe a step change in the e-folding dissolution length scale l_{calc}, in sensitivity simulations This experimental setup is highly idealised. The mechanisms for the dissolution of calcite and other forms of $CaCO_3$ within the water column are quantitatively not well understood. Generally, dissolution of calcite particles within the water column is thought to be linked to low (undersaturated) concentration of carbonate ions in the surrounding water. However, considerable $CaCO_3$ dissolution may occur in the upper ocean (Berelson et al., 2007) in waters that are saturated with respect to calcite or even aragonite, perhaps due to the dissolution of high-magnesium calcite or due to dissolution in specific microenvironments such as zooplankton guts, fecal pellets or organic aggregates (see e.g. Barrett et al., 2014, and references therein). Here, we do not explicitly take into account such effects and the dissolution is for example not affected by changes in the calcite saturation horizon (the depth were the concentration of calcium times the concentration of carbonate equals the solubility product of calcite, Mucci, 1983).

Export fluxes both of POC and calcite remain constant as changes in the dissolution of calcite do not affect productivity. A deepening of l_{calc} (i.e. a lower calcite redissolution rate) leads to an increase of dissolution products – DIC and Alk – in the deep ocean (below ~ 3 km) and a decrease above. This tends to hinder redissolution of calcite from sediment in the deepest layers. Calcite deposition on sediments and burial both increase in response to the increased dissolution length scale. As a consequence, Alk and DIC burial and thus the removal from the ocean increase with a ratio of 2 : 1. In the long run, the balance between weathering input and burial is reestablished by the following process. The removal of Alk and DIC causes an upward shift in the lysocline. In turn, a larger fraction of the calcite deposition flux is redissolved and less is buried.

The ocean inventories of DIC and Alk are both perturbed towards lower values when l_{calc} is increased. This is different to a deepening of the remineralisation depth for POM where the Alk and DIC budgets are perturbed in opposite directions. As a result atmospheric CO_2 is less sensitive to changes in l_{calc} than to changes in l_{POM}. For example, a global deepening of l_{calc} from 2900 m to 3300 m results in an increase in CO_2 by 12.2 ppm in the open system (and only 1.8 ppm in the closed system). Although the absolute sensitivity is lower than for l_{POM}, the amplification by weathering-burial dynamics is even more pronounced with a ~ 7-fold higher response in the open than in the closed system. As oceanic δ^{13}C of DIC is primarily controlled by the organic matter cycle, changes in l_{calc} only marginally influence $^{13}CO_2$ such that the signal is too low to separate it from model-internal variability and drift.

3.3 Sensitivities and sediment feedback quantification

In the following, sensitivities to changes in remineralisation depth are calculated from an experiment where l_{POM} is reduced by 25 m and an experiment where it is increased by 25 m (Table 3). The difference in CO_2 or δ^{13}C between the two experiments is divided by 50 m, the total change in the e-folding depth. This corresponds to a sensitivity calculated symmetrically around the standard (best-guess) value. In general, atmospheric CO_2 responds more sensitive to a shoaling of l_{POM} and l_{calc} than to a deepening. The equilibrium sensitivity of atmospheric CO_2 to changes in $l_{POM} \sim 1.68\,\mathrm{ppm\,m^{-1}}$ in the open system and about 4 times lower, $0.38\,\mathrm{ppm\,m^{-1}}$, in the closed system. Sensitivities in $^{13}CO_2$ (Table 3) are less amplified by the weathering-burial loop due to pCO_2 induced changes in the fractionation factor.

Next, combined changes in l_{POM} and l_{calc} are examined. We sampled the 2-dimensional parameter-space and integrate each model for 20 kyr. To get equilibrium changes in atmospheric CO_2, a linear combination of four exponential functions with different timescales is fitted to the response of the first 20 kyr. The equilibrium response is then found analytically for $t \rightarrow \infty$. The result of this exercise is shown in Fig. 10a and b. As indicated by the green line in Fig. 10b, LGM CO_2 levels could e.g. be reached by changing l_{POM} to ~ 345 m. This number is reduced if l_{calc} is decreased simultaneously. In the closed system on the other hand, LGM CO_2 levels are far from being reconcilable within the bounds of our parameter sampling. The amplification in the response of CO_2 is calculated as the ratio $\Delta pCO_{2,\mathrm{open}}/\Delta pCO_{2,\mathrm{closed}}$ and shown in Fig. 10c. The sediment amplification range is 3–7 for changes in l_{POM} and 7–8 for changes in l_{calc}.

4 Discussion and conclusion

We systematically mapped the spatio-temporal responses for a variety of tracers and proxies to changes in the remineralisation depth of organic matter and calcium carbonate. The Bern3D dynamic ocean model including sediment interactions with organic matter, opal and calcium carbonate is applied. It is shown that ocean–sediment interaction and the weathering-burial cycle strongly amplify the ocean-only response in atmospheric CO_2, $\delta^{13}C$, ocean tracers and particle export fluxes. These processes also lead to sustained changes in whole ocean nutrient and alkalinity inventories. The adjustment to the new steady state occurs on a number of time scales. Ocean only reorganisations take place within decades to centuries and most of the changes in particle export occur within less than 2 kyr, while the adjustment of the phosphate and alkalinity inventories occurs on a typical time scale of about 10–30 kyr. Even longer time scales are involved for the evolution of $\delta^{13}C$. $\delta^{13}C$ signatures are not yet in equilibrium after 200 kyr, the end of our simulations. This implies, as already highlighted by Tschumi et al. (2011) albeit for other mechanisms, that ocean–sediment interactions and the burial-weathering cycles must be considered when discussing the long-term evolution of atmospheric CO_2 and $\delta^{13}C$.

Our model study is associated with a number of limitations. The experiment are idealised and not intended to directly track the evolution of palaeoproxy signals. Changes in remineralisation rates of particulate organic matter (POM) and calcium carbonate ($CaCO_3$) are treated in a parameterised, globally uniform way using a power law and an exponential scaling for the attenuation of POM and $CaCO_3$ fluxes with depth. Further, the Bern3D model is a coarse resolution model with simple parameterisations for the productivity of organic matter, opal, and $CaCO_3$ and fix Redfield ratios are applied. Productivity is linked to phosphate, as well as to iron and silicic acid, but not to nitrogen compounds. Thus, responses in the nitrogen cycle are not taken into account and these may alter in particular the response in export production. Implicitly, the setup corresponds to the assumption that nitrogen fixers make up for the loss of nitrogen by POM burial to the extent needed to support production. The starting point for all sensitivity experiments is a steady state corresponding to preindustrial condition and sensitivity of results may somewhat vary between different background states. A further caveat in our model could be that weathering rates are kept constant. On timescales of several 10 kyr riverine input of tracers are thought to adapt to changes in climatic conditions as well as in pCO_2 (e.g. Colbourn et al., 2013, and references therein). As this negative feedback is not included in our model, the long term response may be overestimated. Slowed bacterial degradation of POM may also imply a change in the mean lifetime of DOM, which we kept constant in our experiment. The impact of a corresponding increase in DOM lifetime is found to weaken the overall response in CO_2 to a change in remineralisation depth of POM by about 15 % (Menviel et al., 2012).

Finally, we did not take into account the radiative feedback associated with altered CO_2 to ease interpretation of results. The climate-carbon feedbacks is positive in our model and its inclusion would yield an even large change in atmospheric CO_2. Despite these numerous caveats, we expect that our experiments provide the first order response to changes in remineralisation depth of POM and $CaCO_3$.

The results show a high sensitivity of atmospheric CO_2 to changes in the POM remineralisation depth. A new element, compared to earlier work with dynamic 3-D ocean models, is that changes in the POM remineralisation rate not only changes the atmosphere–ocean partitioning of carbon, but impacts the long-term carbon cycle by disturbing the weathering-burial balance of carbon, alkalinity and nutrients. This temporary imbalance amplifies the ocean–atmosphere-only response by a factor of ~ 3–7 on multi-millennial time scales. A subtle shift of 1 m (or 4 ‰) in the length scale of POM remineralisation causes a change in atmospheric CO_2 of almost 2 ppm. Our results are quantitative in agreement with Kwon et al. (2009) and Matsumoto (2007) when sediment interactions are neglected. Matsumoto (2007) find a sensitivity in atmospheric CO_2 corresponding to about 7–8 ppm per degree warming and assuming a Q_{10} factor for remineralisation of 2. Kwon et al. (2009) find – for l_{POM} deepening of 24 m – a pCO_2 reduction of 10 ppm using a nutrient restoring formulation of export production (and 27 ppm with constant export) with a model of comparable complexity, but without taking into account ocean–sediment interactions. In our model featuring prognostic export, we find a reduction of 8 ppm in our closed system setup, i.e. without sediment interactions, for l_{POM} deepening of 25 m. In the open system, weathering-burial dynamics increase the response fourfold to 33 ppm. It has been suggested that changes in the rate of $CaCO_3$ dissolution in the upper ocean may be a significant feedback affecting atmospheric CO_2 concentrations and future climatic changes (Barrett et al., 2014). In our sensitivity experiments we varied the e-folding dissolution length scale between 2300 and 3500 m and thereby the amount of $CaCO_3$ dissolution in near surface water and the upper ocean. These variations have a relatively small influence on atmospheric CO_2 in our model on both century (Fig. 10a) and on glacial–interglacial time scales

Title Page
Abstract Introduction
Conclusions References
Tables Figures
◄ ►
◄ ►
Back Close
Full Screen / Esc
Printer-friendly Version
Interactive Discussion

(Fig. 10b). This is consistent with the results of Gangstø et al. (2011) who applied the PISCES ecosystem model with $CaCO_3$ production in the form of calcite and aragonite over the industrial period and in future scenarios. However, these authors restricted the dissolution of $CaCO_3$ to waters that are undersaturated with respect to calcite and aragonite and thus to deeper layers (in particular for calcite) and did not apply a sediment model. Taken together, changes in upper ocean and deep ocean remineralisation rates of $CaCO_3$ appear to exert a small influence on atmospheric CO_2 and thus climate.

The idea of the glacial drawdown of nutrients and carbon from the surface to the deep ocean – either by a more stratified ocean and more sluggish ventilation of the deep ocean or other alterations of the marine biological cycle – and as a consequence the built-up of old respired carbon is widely discussed (Boyle, 1988). Evidence for an increased glacial storage of respired carbon comes from oxygen-sensitive sediment proxies which show that the oxygenation was decreased during glacials. As deep glacial Cd/Ca ratio, a proxy for PO_4, was not increased, these findings lead to the "respired-carbon deepening hypothesis" which denote an increase in remineralised : preformed nutrient supply to the deep ocean (Jaccard et al., 2009; Bradtmiller et al., 2010; Jaccard and Galbraith, 2011). Figure 11 shows the ratio of remineralised : preformed nutrients ($PO_{4,\mathrm{rem}}/PO_{4,\mathrm{pre}}$) in our model – based on apparent oxygen utilisation – as well as the change in this ratio induced by an increase in l_{POM}. A 25 m decrease in the e-folding depth of POM remineralisation leads indeed to a widespread increase in $PO_{4,\mathrm{rem}}/PO_{4,\mathrm{pre}}$ by $\sim 3\,\%$ in the global average. The response in CO_2 to a deepening of the remineralisation depth evolves on time scales that are much longer than the typical duration of the transition from a glacial to an interglacial state, e.g. ≈ 7 ka for termination I. As noted by Menviel et al. (2012), this mechanism can thus not explain, at least not in isolation, the relatively rapid increase in CO_2 over glacial terminations. In agreement, the whole ocean increase in Alk and CO_3^{2-} resulting over long time scales from a deeper remineralisation depth is not observed in proxy records, which show little glacial–interglacial changes in CO_3^{2-} (Yu et al., 2010, 2013).

The results confirm that the nutrient-burial feedback identified by Tschumi et al. (2011) should not be neglected (e.g. Sigman et al., 1998; Matsumoto et al., 2007; Chikamoto et al., 2008) when discussing long-term carbon cycle changes. This nutrient-burial feedback arises as marine biological productivity in the long run is limited by the riverine or aeolian input of nutrients into the ocean. The burial flux, not only of $CaCO_3$ but also of POM must relax to the input flux of tracers into the ocean. This nutrient-burial feedback amplifies the initial response to a deepening of the POM remineralisation by a factor between three and seven in our model. There are small changes in $\Delta^{14}C$ in the atmosphere and the ocean in our POM deepening experiments. On the other hand, we find substantial changes in alkalinity, DIC, oxygen, and atmospheric CO_2. This suggests that the relationship between $\Delta^{14}C$ and DIC observed in the modern ocean (Sarnthein et al., 2013), may not always be applicable to infer changes in DIC from changes in $\Delta^{14}C$.

The response of the carbon cycle to complex forcings may be approximated using an impulse response-empirical orthogonal function representation. To this end, we find that the spatio-temporal response of a variety of tracers to a step change in remineralisation depth, can be accurately approximated by the first two or three principal components and the associated spatial patterns. This holds even for $\delta^{13}C$ of DIC, despite that its evolution is governed by a range of processes involving different time scales. The implication is that a complex carbon cycle model may be substituted by a cost-efficient impulse response-empirical orthogonal function representation within the quasi-linear regime. This may facilitate simulations over many millions of years or Monte Carlo type applications for a range of forcing evolutions.

We have shown that a change in the rate of organic matter degradation constitutes an important potential feedback for atmospheric CO_2 to temperature change. Small changes in the remineralisation depth lead to surprisingly large changes in atmospheric CO_2 and related tracers in particular over glacial–interglacial time scales. While the available proxy records do not support the conclusion that a deepening in the POM remineralisation depth played a dominant role for the CO_2 increase during the last termination, the high sensitivity implies that subtle changes in the remineralisation depth on global to regional scales cannot be easily disregarded for the explanation of the long-term evolution of atmospheric CO_2 and $\delta^{13}C$, the distribution of nutrients, alkalinity, oxygen, carbonate ions or $\delta^{13}C$ within the ocean, as well as for marine productivity, particle fluxes, and sedimentation.

Appendix A

Bern3D model update

Recently, the physical core of the Bern3D ocean component underwent some major changes. Before this update, only horizontal grids with a latitudinal spacing proportional to the sine of the latitude were possible, such that the surface area of all gridboxes is equal. Based on this constraint, many equations were simplified in the original Bern3D model (Müller et al., 2006) (which in turn is based on the GOLDSTEIN model, Edwards and Marsh, 2005) as gridcell areas were omitted in the equations.

All equations were generalised to be used with arbitrary rectangular grids. Several horizontal grid configurations were tested in an early stage. A grid with 41 × 40 gridboxes in the horizontal featuring a higher latitudinal resolution in the Southern Ocean as well as an increased longitudinal resolution in the Atlantic has been chosen. The old and new grids are shown in Fig. A2. This particular 41 × 40 grid offers a good balance between computational efficiency and increased resolution in important locations. Although the number of boxes only modestly increased, the timestep (δt) had to be decreased by a factor of two in order to maintain numerical stability.

In addition to the horizontal resolution, some minor changes were incorporated in the ocean, EBM and biogeochemical modules as described in the following. As a result of a proper re-tuning of all model components, there is some notable improvement in the modelled ocean distribution of tracers, as illustrated in the Taylor diagram shown in

Fig. A1. For a more detailed description and the present day solution see Roth (2013, Chap. 2).

A1 Physical component

The following changes in the physical part were made (parameters w.r.t. the 36 × 36 setup as described in Ritz et al., 2011a and updated in Ritz et al., 2011b):

- new grid with 41 × 40 gridboxes in the horizontal.
- Ocean:
  - new parameter set (see Table A1)
  - new time step: 96 timesteps per year (instead of 48 timesteps per year in the old version)
  - max. isopycnal slope has been increased to prevent spatial oscillations of the tracer fields in the Southern Ocean
  - shuffling convection is now applied for all tracers (instead of only to T & S).
- Atmosphere:
  - new parameter set (see Table A1)
  - no Atlantic-to-Pacific freshwater correction flux
  - zonal resolved winds are now used for moisture and heat advection
  - zonal eddy-diffusive transport of heat is now a function of latitude (see Table A1)
  - moisture advection is now reduced by a scaling factor $\beta_{\text{moist}} = 0.5$
  - land albedo changes through snow is now taken into account by default. Changes in snow albedo calculated by the snow albedo parametrisation of Ritz et al. (2011b) are accounted for as anomalies to the fixed surface albedo.

    Minimum snow albedo is the MODIS[1] land surface albedo from which the snow contribution has been removed
  - air–sea momentum transfer (i.e. wind stress) is reduced by fractional sea-ice cover (F_{ice}) by a factor of ($1 - F_{\text{ice}}^2$).

- Sea ice:
  - sea ice is solved with a separate time-stepping: 10 steps per atmospheric time step
  - sea ice advection is reduced to 0.3 times the surface ocean current for better consistency with observations.

- Ice sheet:
  - new ice-sheet parametrisation: Greenland and Antarctica are now assumed to have temporally constant ice sheet cover. Due to this, the climate is no longer affected when ice sheets are activated at a present day state (albedo of Greenland and Antarctica remain at the values of the MODIS climatology)
  - updated ice-sheet mask (Peltier, 2004).

In the 41 × 40 version, the key ocean parameters remained largely unchanged with the exception of an ad-hoc doubling of diapycnal diffusivity (k_D) from $10^{-5}\,\text{m}^2\,\text{s}^{-1}$ to $2 \times 10^{-5}\,\text{m}^2\,\text{s}^{-1}$. This change was motivated by the lower-than-observed rates of anthropogenic CO_2 uptake in the old model version (Gerber and Joos, 2013). With the new model the cumulative uptake of CO_2 from 1765–2011 AD is 156 GtC which compares well with observational estimates of 155 ± 31 GtC (Le Quéré et al., 2013).

---

[1] The Moderate Resolution Imaging Spectroradiometer.

A2 Biogeochemical component

The following changes in the biogeochemical component were made (parameters w.r.t. the 36 × 36 setup as described in Parekh et al., 2008; Tschumi et al., 2008, 2011):

- Ocean biogeochemistry:
  - new parameter set (see Table A2)
  - new windspeed climatology (from NCEP instead of PO.DACC) for the gas exchange formulation
  - new present-day dust input fields from Mahowald et al. (2006)
  - virtual fluxes are now applied to all biogeochemical tracers.
- Sediment:
  - new parameter set (see Table A2)
  - Alk : P ratio for organic matter formation and remineralisation is set to −17 according to Paulmier et al. (2009)
  - weathering input is now distributed along the coastline instead of the entire surface ocean
  - organic matter denitrification disabled per default to avoid model drift.

Acknowledgements. This work is supported by the European Commission through the Seventh Framework Program (FP7) projects CARBOCHANGE (grant no. 264879) and Past4Future (grant no. 243908) and the Swiss National Science Foundation.

References

Antonov, J. I., Seidov, D., Boyer, T. P., Locarnini, R. A., Mishonov, A. V., Garcia, H. E., Baranova, O. K., Zweng, M. M., and Johnson, D. R.: World Ocean Atlas 2009, Volume 2: Salinity, NOAA Atlas NESDIS 69, US Government Printing Office, Washington, D.C., 2010. 481

Archer, D., Winguth, A., Lea, D., and Mahowald, N.: What caused the glacial/interglacial atmospheric $p\mathrm{CO}_2$ cycles?, Rev. Geophys., 38, 159–189, doi:10.1029/1999RG000066, 2000. 474

Armstrong, R. A., Lee, C., Hedges, J. I., Honjo, S., and Wakeham, S. G.: A new, mechanistic model for organic carbon fluxes in the ocean based on the quantitative association of POC with ballast minerals, Deep-Sea Res. Pt. II, 49, 219–236, doi:10.1016/S0967-0645(01)00101-1, 2002. 475

Armstrong, R. A., Peterson, M. L., Lee, C., and Wakeham, S. G.: Settling velocity spectra and the ballast ratio hypothesis, Deep-Sea Res. Pt. II, 56, 1470–1478, doi:10.1016/j.dsr2.2008.11.032, 2009. 475

Arora, V. K., Boer, G. J., Friedlingstein, P., Eby, M., Jones, C. D., Christian, J. R., Bonan, G., Bopp, L., Brovkin, V., Cadule, P., Hajima, T., Ilyina, T., Lindsay, K., Tjiputra, J. F., and Wu, T.: Carbon–concentration and carbon–climate feedbacks in CMIP5 Earth System Models, J. Climate, 26, 5289–5314, doi:10.1175/JCLI-D-12-00494.1, 2013. 483

Barrett, P. M., Resing, J. A., Buck, N. J., Feely, R. A., Bullister, J. L., Buck, C. S., and Landing, W. M.: Calcium carbonate dissolution in the upper 1000 m of the eastern North Atlantic, Global Biogeochem. Cy., doi:10.1002/2013GB004619, in press, 2014. 492, 496

Bendtsen, J., Lundsgaard, C., Middelboe, M., and Archer, D.: Influence of bacterial uptake on deep-ocean dissolved organic carbon, Global Biogeochem. Cy., 16, 1127, doi:10.1029/2002GB001947, 2002. 475

Berelson, W. M., Balch, W. M., Najjar, R., Feely, R. A., Sabine, C., and Lee, K.: Relating estimates of CaCO_3 production, export, and dissolution in the water column to measurements of CaCO_3 rain into sediment traps and dissolution on the sea floor: a revised global carbonate budget, Global Biogeochem. Cy., 21, GB1024, doi:10.1029/2006GB002803, 2007. 492

Bouttes, N., Paillard, D., and Roche, D. M.: Impact of brine-induced stratification on the glacial carbon cycle, Clim. Past, 6, 575–589, doi:10.5194/cp-6-575-2010, 2010. 475

Boyle, E. A.: Vertical oceanic nutrient fractionation and glacial/interglacial CO_2 cycles, Nature, 331, 55–56, doi:10.1038/331055a0, 1988. 497

Bradtmiller, L., Anderson, R., Sachs, J., and Fleisher, M.: A deeper respired carbon pool in the glacial equatorial Pacific Ocean, Earth Planet. Sc. Lett., 299, 417–425, doi:10.1016/j.epsl.2010.09.022, 2010. 497

Chikamoto, M. O., Matsumoto, K., and Ridgwell, A.: Response of deep-sea $CaCO_3$ sedimentation to Atlantic meridional overturning circulation shutdown, J. Geophys. Res., 113, G03017, doi:10.1029/2007JG000669, 2008. 498

Chikamoto, M. O., Abe-Ouchi, A., Oka, A., and Smith, S. L.: Temperature-induced marine export production during glacial period, Geophys. Res. Lett., 39, L21601, doi:10.1029/2012GL053828, 2012. 475

Colbourn, G., Ridgwell, A., and Lenton, T. M.: The Rock Geochemical Model (RokGeM) v0.9, Geosci. Model Dev., 6, 1543–1573, doi:10.5194/gmd-6-1543-2013, 2013. 495

Denman, K. L., Brasseur, G., Chidthaisong, A., Ciais, P., Cox, P. M., Dickinson, R. E., Hauglustaine, D., Heinze, C., Holland, E., Jacob, D., Lohmann, U., Ramachandran, S., da Silva Dias, P. L., Wofsy, S. C., and Zhang, X.: Couplings between changes in the climate system and biogeochemistry, in: Climate Change 2007: The Physical Science Basis, Working Group I Contribution to the Fourth Assessment Report of the Intergovernmental Panel on Climate Change, edited by: Solomon, S., Qin, D., Manning, M., Chen, Z., Marquis, M., Averyt, K. B., Tignor, M., and Miller, H. L., Cambridge University Press, Cambridge, UK and New York, NY, USA, 499–588, 2007.

Doney, S. C., Lindsay, K., Fung, I., and John, J.: Natural variability in a stable, 1000-yr global coupled climate–carbon cycle simulation, J. Climate, 19, 3033–3054, doi:10.1175/JCLI3783.1, 2006. 478

Edwards, N. R. and Marsh, R.: Uncertainties due to transport-parameter sensitivity in an efficient 3-D ocean-climate model, Clim. Dynam., 24, 415–433, doi:10.1007/s00382-004-0508-8, 2005. 477, 478, 499

Feely, R., Sabine, C., Lee, K., Berelson, W., Kleypas, J., Fabry, V., and Millero, F.: Impact of anthropogenic CO_2 on the $CaCO_3$ system in the oceans, Science, 305, 362–366, doi:10.1126/science.1097329, 2004. 511

Fischer, H., Schmitt, J., Lüthi, D., Stocker, T. F., Tschumi, T., Parekh, P., Joos, F., Köhler, P., Völker, C., Gersonde, R., Barbante, C., Le Floch, M., Raynaud, D., and Wolff, E. W.: The role of Southern Ocean processes on orbital and millenial CO_2 variations – a synthesis, Quaternary Sci. Rev., 29, 193–205, doi:10.1016/j.quascirev.2009.06.007, 2010. 474

Freeman, K. H. and Hayes, J. M.: Fractionation of carbon isotopes by phytoplankton and estimates of ancient CO_2 levels, Global Biogeochem. Cy., 6, 185–198, doi:10.1029/92GB00190, 1992. 479, 491

Gangstø, R., Joos, F., and Gehlen, M.: Sensitivity of pelagic calcification to ocean acidification, Biogeosciences, 8, 433–458, doi:10.5194/bg-8-433-2011, 2011. 497

Gehlen, M., Bopp, L., Emprin, N., Aumont, O., Heinze, C., and Ragueneau, O.: Reconciling surface ocean productivity, export fluxes and sediment composition in a global biogeochemical ocean model, Biogeosciences, 3, 521–537, doi:10.5194/bg-3-521-2006, 2006. 480

Gerber, M. and Joos, F.: An Ensemble Kalman Filter multi-tracer assimilation: determining uncertain ocean model parameters for improved climate-carbon cycle projections, Ocean Model., 64, 29–45, doi:10.1016/j.ocemod.2012.12.0, 2013. 501

Griffies, S. M.: The Gent–McWilliams skew flux, J. Phys. Oceanogr., 28, 831–841, doi:10.1175/1520-0485(1998)028<0831:TGMSF>2.0.CO;2, 1998. 478

Heinze, C., Maier-Reimer, E., Winguth, A. M. E., and Archer, D.: A global oceanic sediment model for long-term climate studies, Global Biogeochem. Cy., 13, 221–250, 1999. 480

Hibler, W.: A dynamic thermodynamic sea ice model, J. Phys. Oceanogr., 9, 815–846, doi:10.1175/1520-0485(1979)009<0815:ADTSIM>2.0.CO;2, 1979. 478

Hooss, G., Voss, R., Hasselmann, K., Maier-Reimer, E., and Joos, F.: A nonlinear impulse response model of the coupled carbon cycle-climate system (NICCS), Clim. Dynam., 18, 189–202, doi:10.1007/s003820100170, 2001. 484

Huybers, P. and Langmuir, C.: Feedback between deglaciation, volcanism, and atmospheric CO_2, Earth Planet. Sc. Lett., 286, 479–491, doi:10.1016/j.epsl.2009.07.014, 2009. 475

Jaccard, S. L. and Galbraith, E. D.: Large climate-driven changes of oceanic oxygen concentrations during the last deglaciation, Nat. Geosci., 5, 151–156, doi:10.1038/ngeo1352, 2011. 497

Jaccard, S. L., Galbraith, E., Sigman, D., Haug, G., Francois, R., Pedersen, T., Dulski, P., and Thierstein, H.: Subarctic Pacific evidence for a glacial deepening of the oceanic respired carbon pool, Earth Planet. Sc. Lett., 277, 156–165, doi:10.1016/j.epsl.2008.10.017, 2009. 497

Jin, X., Gruber, N., Dunne, J. P., Sarmiento, J. L., and Armstrong, R. A.: Diagnosing the contribution of phytoplankton functional groups to the production and export of particulate organic carbon, $CaCO_3$, and opal from global nutrient and alkalinity distributions, Global Biogeochem. Cy., 20, GB2015, doi:10.1029/2005GB002532, 2006. 511

Joos, F., Bruno, M., Fink, R., Siegenthaler, U., Stocker, T. F., Le Quéré, C., and Sarmiento, J.: An efficient and accurate representation of complex oceanic and biospheric models of anthropogenic carbon uptake, Tellus B, 48, 397–417, doi:10.1034/j.1600-0889.1996.t01-2-00006.x, 1996. 484

Joos, F., Plattner, G.-K., Stocker, T. F., Marchal, O., and Schmittner, A.: Global warming and marine carbon cycle feedbacks on future atmospheric CO_2, Science, 284, 464–467, doi:10.1126/science.284.5413.464, 1999. 483

Kalnay, E., Kanamitsu, M., Kistler, R., Collins, W., Deaven, D., Gandin, L., Iredell, M., Saha, S., White, G., Woollen, J., Zhu, Y., Chelliah, M., Ebisuzaki, W., Higgins, W., Janowiak, J., Mo, K., Ropelewski, C., Wang, J., Leetmaa, A., Reynolds, R., Jenne, R., and Joseph, D.: The NCEP/NCAR 40-year reanalysis project, B. Am. Meteorol. Soc., 77, 437–471, doi:10.1175/1520-0477(1996)077<0437:TNYRP>2.0.CO;2, 1996. 478

Key, R. M., Kozyr, A., Sabine, C. L., Lee, K., Wanninkhof, R., Bullister, J. L., Feely, R. A., Millero, F. J., Mordy, C., and Peng, T.-H.: A global ocean carbon climatology: results from Global Data Analysis Project (GLODAP), Global Biogeochem. Cy., 18, GB4031, doi:10.1029/2004GB002247, 2004. 481

Kwon, E. Y., Primeau, F., and Sarmiento, J. L.: The impact of remineralization depth on the air–sea carbon balance, Nat. Geosci., 2, 630–635, doi:10.1038/ngeo612, 2009. 475, 482, 496

Le Quéré, C., Andres, R. J., Boden, T., Conway, T., Houghton, R. A., House, J. I., Marland, G., Peters, G. P., van der Werf, G. R., Ahlström, A., Andrew, R. M., Bopp, L., Canadell, J. G., Ciais, P., Doney, S. C., Enright, C., Friedlingstein, P., Huntingford, C., Jain, A. K., Jourdain, C., Kato, E., Keeling, R. F., Klein Goldewijk, K., Levis, S., Levy, P., Lomas, M., Poulter, B., Raupach, M. R., Schwinger, J., Sitch, S., Stocker, B. D., Viovy, N., Zaehle, S., and Zeng, N.: The global carbon budget 1959–2011, Earth Syst. Sci. Data, 5, 165–185, doi:10.5194/essd-5-165-2013, 2013. 501

Locarnini, R. A., Mishonov, A. V., Antonov, J. I., Boyer, T. P., Garcia, H. E., Baranova, O. K., Zweng, M. M., and Johnson, D. R.: World Ocean Atlas 2009, Volume 1: Temperature, NOAA Atlas NESDIS 68, US Government Printing Office, Washington, D.C., 2010. 481

Lüthi, D., Le Floch, M., Bereiter, B., Blunier, T., Barnola, J.-M., Siegenthaler, U., Raynaud, D., Jouzel, J., Fischer, H., Kawamura, K., and Stocker, T. F.: High-resolution carbon dioxide concentration record 650,000–800,000 years before present, Nature, 453, 379–382, doi:10.1038/nature06949, 2008. 474

Mahowald, N. M., Muhs, D. R., Levis, S., Rasch, P. J., Yoshioka, M., Zender, C. S., and Luo, C.: Change in atmospheric mineral aerosols in response to climate: last glacial period, preindustrial, modern, and doubled carbon dioxide climates, J. Geophys. Res., 111, D10202, doi:10.1029/2005JD006653, 2006. 502

Martin, J. H., Knauer, G. A., Karl, D. M., and Broenkow, W.: VERTEX: carbon cycling in the northeast Pacific, Deep-Sea Res. Part I, 34, 267–285, doi:10.1016/0198-0149(87)90086-0, 1987. 479

Matsumoto, K.: Biology-mediated temperature control on atmospheric $p\mathrm{CO_2}$ and ocean biogeochemistry, Geophys. Res. Lett., 34, L20605, doi:10.1029/2007GL031301, 2007. 475, 496

Matsumoto, K., Hashioka, T., and Yamanaka, Y.: Effect of temperature-dependent organic carbon decay on atmospheric $p\mathrm{CO_2}$, J. Geophys. Res., 112, G02007, doi:10.1029/2006JG000187, 2007. 475, 476, 498

Menviel, L., Joos, F., and Ritz, S.: Simulating atmospheric CO_2, ^{13}C and the marine carbon cycle during the Last Glacial–Interglacial cycle: possible role for a deepening of the mean remineralization depth and an increase in the oceanic nutrient inventory, Quaternary Sci. Rev., 56, 46–68, doi:10.1016/j.quascirev.2012.09.012, 2012. 476, 495, 497

Milliman, J. and Droxler, A.: Neritic and pelagic carbonate sedimentation in the marine environment: ignorance is not bliss, Geol. Rundsch., 85, 496–504, doi:10.1007/BF02369004, 1996. 511

Mucci, A.: The solubility of calcite and aragonite in seawater at various salinities, temperatures, and one atmosphere total pressure, Am. J. Sci., 283, 780–799, 1983. 493

Müller, S. A., Joos, F., Edwards, N. R., and Stocker, T. F.: Water mass distribution and ventilation time scales in a cost-efficient, three-dimensional ocean model, J. Climate, 19, 5479–5499, doi:10.1175/JCLI3911.1, 2006. 477, 499

Müller, S. A., Joos, F., Edwards, N. R., and Stocker, T. F.: Modeled natural and excess radiocarbon: sensitivities to the gas exchange formulation and ocean transport strength, Global Biogeochem. Cy., 22, GB3011, doi:10.1029/2007GB003065, 2008. 478

Munhoven, G.: Glacial-interglacial changes of continental weathering: estimates of the related CO_2 and HCO_3^- flux variations and their uncertainties, Global Planet. Change, 33, 155–176, doi:10.1016/s0921-8181(02)00068-1, 2002. 475

Najjar, R. G., Orr, J., Sabine, C. L., and Joos, F.: Biotic-HOWTO, Internal OCMIP Report, Tech. rep., LSCE/CEA Saclay, Gif-sur-Yvette, France, 1999. 478

Oka, A., Abe-Ouchi, A., Chikamoto, M. O., and Ide, T.: Mechanisms controlling export production at the LGM: effects of changes in oceanic physical fields and atmospheric dust deposition, Global Biogeochem. Cy., 25, GB2009, doi:10.1029/2009GB003628, 2011. 475

Orr, J. and Najjar, R. G.: Abiotic-HOWTO, Internal OCMIP Report, Tech. rep., LSCE/CEA Saclay, Gif-sur-Yvette, France, 1999. 478

Parekh, P., Joos, F., and Müller, S. A.: A modeling assessment of the interplay between aeolian iron fluxes and iron-binding ligands in controlling carbon dioxide fluctuations during Antarctic warm events, Paleoceanography, 23, PA4202, doi:10.1029/2007PA001531, 2008. 475, 478, 502

Paulmier, A., Kriest, I., and Oschlies, A.: Stoichiometries of remineralisation and denitrification in global biogeochemical ocean models, Biogeosciences, 6, 923–935, doi:10.5194/bg-6-923-2009, 2009. 502

Peltier, W. R.: Global glacial isostasy and the surface of the Ice-Age Earth: the ICE-5G (VM2) model and GRACE, Annu. Rev. Earth Pl. Sc., 32, 111–149, doi:10.1146/annurev.earth.32.082503.144359, 2004. 501

Petit, J. R., Jouzel, J., Raynaud, D., Barkov, N. I., Barnola, J.-M., Basile, I., Bender, M., Chappellaz, J., Davis, M., Delaygue, G., Delmotte, M., Kotlyakov, V. M., Legrand, M., Lipenkov, V. Y., Lorius, C., PEpin, L., Ritz, C., Saltzman, E., and Stievenard, M.: Climate and atmospheric history of the past 420,000 years from the Vostok ice core, Antarctica, Nature, 399, 429–436, doi:10.1038/20859, 1999. 474

Plattner, G.-K., Knutti, R., Joos, F., Stocker, T. F., von Bloh, W., Brovkin, V., Cameron, D., Driesschaert, E., Dutkiewiz, S., Eby, M., Edwards, N. R., Fichefet, T., Hargreaves, J. C., Jones, C. D., Loutre, M. F., Matthews, H. D., Mouchet, A., Müller, S. A., Nawrath, S., Price, A., Sokolov, A., Strassmann, K. M., and Weaver, A. J.: Long-term climate commitments projected with climate–carbon cycle models, J. Climate, 21, 2721–2751, doi:10.1175/2007JCLI1905.1, 2008. 483

Ritz, S. P., Stocker, T. F., and Joos, F.: A coupled dynamical ocean-energy balance atmosphere model for paleoclimate studies, J. Climate, 24, 349–375, doi:10.1175/2010JCLI3351.1, 2011a. 478, 500, 514

Ritz, S. P., Stocker, T. F., and Severinghaus, J. P.: Noble gases as proxies of mean ocean temperature: sensitivity studies using a climate model of reduced complexity, Quaternary Sci. Rev., 30, 3728–3741, doi:10.1016/j.quascirev.2011.09.021, 2011b. 500

Roth, R.: Modeling forcings and responses in the global carbon cycle–climate system: past, present and future, Ph.D. thesis, University of Bern, Bern, 2013. 500

Roth, R. and Joos, F.: Model limits on the role of volcanic carbon emissions in regulating glacial-interglacial CO_2 variations, Earth Planet. Sc. Lett., 329–330, 141–149, doi:10.1016/j.epsl.2012.02.019, 2012. 475

Sarmiento, J. L. and Gruber, N.: Ocean Biogeochemical Dynamics, Princeton University Press, Princeton, Oxford, 2006. 511

Sarnthein, M., Schneider, B., and Grootes, P. M.: Peak glacial ^{14}C ventilation ages suggest major draw-down of carbon into the abyssal ocean, Clim. Past, 9, 2595–2614, doi:10.5194/cp-9-2595-2013, 2013. 498

Schneider, B., Bopp, L., and Gehlen, M.: Assessing the sensitivity of modeled air–sea CO_2 exchange to the remineralization depth of particulate organic and inorganic carbon, Global Biogeochem. Cy., 22, GB3021, doi:10.1029/2007GB003100, 2008. 482

Segschneider, J. and Bendtsen, J.: Temperature-dependent remineralization in a warming ocean increases surface $p\mathrm{CO}_2$ through changes in marine ecosystem composition, Global Biogeochem. Cy., 27, GB004684, doi:10.1002/2013GB004684, 2013. 475

Semtner, A. J.: A model for the thermodynamic growth of sea ice in numerical investigations of climate, J. Phys. Oceanogr., 6, 379–389, doi:10.1175/1520-0485(1976)006<0379:AMFTTG>2.0.CO;2, 1976. 478

Siegenthaler, U., Stocker, T. F., Monnin, E., Lüthi, D., Schwander, J., Stauffer, B., Raynaud, D., Barnola, J.-M., Fischer, H., Masson-Delmotte, V., and Jouzel, J.: Stable carbon cycle–climate relationship during the Late Pleistocene, Science, 310, 1313–1317, doi:10.1126/science.1120130, 2005. 474

Sigman, D. M. and Boyle, E. A.: Glacial/interglacial variations in atmospheric carbon dioxide, Nature, 407, 859–869, doi:10.1038/35038000, 2000. 474

Sigman, D. M., McCorkle, D. C., and Martin, W. R.: The calcite lysocline as a constraint on glacial/interglacial low-latitude production changes, Global Biogeochem. Cy., 12, 409–427, doi:10.1029/98GB01184, 1998. 498

Sigman, D. M., Hain, M. P., and Haug, G. H.: The polar ocean and glacial cycles in atmospheric CO_2 concentration, Nature, 466, 47–55, doi:10.1038/nature09149, 2010. 474

Steinacher, M., Joos, F., Frölicher, T. L., Bopp, L., Cadule, P., Cocco, V., Doney, S. C., Gehlen, M., Lindsay, K., Moore, J. K., Schneider, B., and Segschneider, J.: Projected

21st century decrease in marine productivity: a multi-model analysis, Biogeosciences, 7, 979–1005, doi:10.5194/bg-7-979-2010, 2010. 482

Taucher, J., Bach, L., Riebesell, U., and Oschlies, A.: The viscosity effect on marine particle flux – a climate relevant feedback mechanism, Global Biogeochem. Cy., doi:10.1002/2013GB004728, in press, 2014. 475

Thompson, S. L. and Warren, S. G.: Parameterization of outgoing infrared radiation derived from detailed radiative calculations, J. Atmos. Sci., 39, 2667–2680, 1982. 478

Tréguer, P., Nelson, D. M., Van Bennekom, A. J., DeMaster, D. J., Leynaert, A., and Quéguiner, B.: The silica balance in the World Ocean: a reestimate, Science, 268, 375–379, doi:10.1126/science.268.5209.375, 1995. 511

Tschumi, T., Joos, F., and Parekh, P.: How important are Southern Hemisphere wind changes for low glacial carbon dioxide? A model study, Paleoceanography, 23, PA4208, doi:10.1029/2008PA001592, 2008. 502

Tschumi, T., Joos, F., Gehlen, M., and Heinze, C.: Deep ocean ventilation, carbon isotopes, marine sedimentation and the deglacial CO_2 rise, Clim. Past, 7, 771–800, doi:10.5194/cp-7-771-2011, 2011. 475, 476, 477, 478, 481, 495, 498, 502, 515

Völker, C. and Köhler, P.: Responses of ocean circulation and carbon cycle to changes in the position of the Southern Hemisphere westerlies at Last Glacial Maximum, Paleoceanography, 28, 726–739, doi:10.1002/2013PA002556, 2013. 475

Watson, A. and Garabato, A.: The role of Southern Ocean mixing and upwelling in glacial–interglacial atmospheric CO_2 change, Tellus B, 58, 73–87, doi:10.1111/j.1600-0889.2005.00167.x, 2006. 475

Weaver, A. J., Eby, M., Wiebe, E. C., Bitz, C. M., Duffy, P. B., Ewen, T. L., Fanning, A. F., Holland, M. M., MacFadyen, A., Wang, H. X., and Yoshimori, M.: The UVic Earth System Climate Model: model description, climatology, and applications to past, present and future climates, Atmos. Ocean, 39, 361–428, doi:10.1080/07055900.2001.9649686, 2001. 478

Yu, J., Broecker, W. S., Elderfield, H., Jin, Z., McManus, J., and Zhang, F.: Loss of carbon from the deep sea since the Last Glacial Maximum, Science, 330, 1084–1087, doi:10.1126/science.1193221, 2010. 497

Yu, J., Anderson, R. F., Jin, Z., Rae, J. W., Opdyke, B. N., and Eggins, S. M.: Responses of the deep ocean carbonate system to carbon reorganization during the last glacial–interglacial cycle, Quaternary Sci. Rev., 76, 39–52, doi:10.1016/j.quascirev.2013.06.020, 2013. 497

Table 1. Overview on globally integrated particle fluxes for a preindustrial control simulation.

variable	units	value	range of estimates
ocean inventory:			
DIC	GtC	37 370	37 510[a]
export:			
$CaCO_3$	$GtC\,yr^{-1}$	0.872	0.8–1.2[b]
opal	$Tmol\,Si\,yr^{-1}$	101	102–178[b]
POM	$GtC\,yr^{-1}$	11.7	6.5–13.1[c]
deposition:			
$CaCO_3$	$GtC\,yr^{-1}$	0.273	0.5[f]
opal	$Tmol\,Si\,yr^{-1}$	70.2	13–47[e]
POM	$GtC\,yr^{-1}$	0.630	1.7–3.3[c]
burial:			
$CaCO_3$	$GtC\,yr^{-1}$	0.0916	0.10–0.14[d]
opal	$Tmol\,Si\,yr^{-1}$	2.11	5.3–8.9[e]
POM	$GtC\,yr^{-1}$	0.181	0.12–0.26[c]
ocean tracer weathering/burial fluxes:			
PO_4	$Tmol\,P\,yr^{-1}$	0.130	
DIC	$GtC\,yr^{-1}$	0.273	
$\delta^{13}C$	‰	−12.6	
Alk	$Teq\,yr^{-1}$	13.1	
Silicate	$Tmol\,Si\,yr^{-1}$	2.11	

[a] Based on the GLODAP and WOA09 datasets.
[b] Jin et al. (2006)
[c] Sarmiento and Gruber (2006)
[d] Feely et al. (2004) (excluding continental shelf areas)
[e] Tréguer et al. (1995)
[f] Milliman and Droxler (1996).

Table 2. Changes in atmospheric pCO_2 induced by a global/regional deepening of the depth scale (l_{POM}) from 250 m (control) to 275 m in the open system. Negative numbers denote a decrease in pCO_2.

Region	ΔpCO_2 (ppm)	ΔpCO_2 (ppm) normalised by area[a]	ΔpCO_2 (ppm) normalised by export[b]
Global	−33.4	−33.4	−33.4
90–30° N	−6.9	−39.5	−50.1
30° N–30° S	−19.8	−37.7	−35.9
30–90° S	−8.9	−29.5	−28.5

[a] The fractional sea surface areas are: 90–30° N: 17 %, 30° N–30° S: 52 %, 30–90° S: 30 %.

[b] The fractional export fluxes are: 90–30° N: 14 %, 30° N–30° S: 55 %, 30–90° S: 31 %.

Table 3. Equilibrium changes in atmospheric pCO_2 and $^{13}CO_2$ (expressed as $\delta^{13}C$) induced by a global change in the mean remineralisation depth of POM and calcite redissolution length-scale.

	closed system		open system	
	ΔpCO_2	$\Delta\delta^{13}CO_2$	ΔpCO_2	$\Delta\delta^{13}CO_2$[a]
l_{POM}: 250 m → 275 m	−8.1 ppm	0.037 ‰	−33.4 ppm	0.084 ‰
l_{POM}: 250 m → 225 m	10.8 ppm	−0.046 ‰	50.4 ppm	−0.10 ‰
sensitivity	$0.38\,\mathrm{ppm\,m^{-1}}$	$-0.0017\,‰\,\mathrm{m^{-1}}$	$1.68\,\mathrm{ppm\,m^{-1}}$	$-0.0037\,‰\,\mathrm{m^{-1}}$
l_{calc}: 2900 m → 3300 m	1.8 ppm	–[b]	12.2 ppm	–[b]
l_{calc}: 2900 m → 2500 m	−2.1 ppm	–[b]	−14.6 ppm	–[b]
sensitivity	$0.0049\,\mathrm{ppm\,m^{-1}}$	–[b]	$0.034\,\mathrm{ppm\,m^{-1}}$	–[b]

[a] Maximum anomaly is stated (i.e. after ~ 10–15 kyr).

[b] Changes in $\delta^{13}CO_2$ are too small to be separated from model drift.

Table A1. Parameters in the ocean (OCN) and energy-balance atmosphere (EBM) modules that changed with respect to the parameters listed in Ritz et al. (2011a).

module	parameter	new value	units	description
OCN	k_D	2×10^{-5}	$\mathrm{m^2\,s^{-1}}$	diapycnal diffusivity
OCN	$\mathrm{fw_{SO}}$	0.07	Sv	Weddell sea freshwater removal
OCN	$\mathrm{fw_{Atl\text{-}Pac}}$	0.0	Sv	Atlantic to Pacific freshwater flux correction
OCN	$\mathrm{ss_{max}}$	40	–	slope limitation of isopycnals
EBM	ε_l	1.00	–	reference land emissivity
EBM	G_cl	0.219	–	fraction of shortwave radiation that is reflected by the atmosphere in the standard case for clear sky conditions
EBM	G_ov	0.379	–	fraction of shortwave radiation that is reflected by the atmosphere in the standard case for overcast conditions
EBM	λ_rad	0.641	–	ratio between the total transmissivity in overcast and clear-sky conditions for the standard cases
EBM	$r_\mathrm{h,precip}$	0.85	–	relative humidity after precipitation
EBM	K_φ	$2.0\times10^5+(2.0\times10^7-2.0\times10^5)\times\cos^4\vartheta$	$\mathrm{m^2\,s^{-1}}$	zonal eddy-diffusivity of heat
EBM	K_ϑ	$1.2\times10^6+0.6\times10^6\frac{\vartheta+\pi/2}{\pi}+2.5\times10^6\cos^2\vartheta$	$\mathrm{m^2\,s^{-1}}$	meridional eddy-diffusivity of heat
EBM	β_moist	0.5	–	scaling coefficient for moisture advection
EBM	$\lambda_\mathrm{lw\_rad}$	-0.71	$\mathrm{W\,m^{-2}\,K^{-1}}$	Feedback parameter
EBM	K_i	1.5×10^4	$\mathrm{m^2\,s^{-1}}$	sea-ice diffusion coefficient
EBM	β_ice	0.3	–	scaling coefficient for sea-ice advection
EBM	α_seaice	0.65	–	sea-ice albedo
EBM	α_icesheet	0.7	–	ice-sheet albedo
EBM	$\alpha_\mathrm{snow}^\mathrm{max}$	0.75	–	maximum snow albedo
EBM	H_0	0.05	m	minimal ice thickness

Table A2. Overview on updated parameters in the 41 × 40 setup of the ocean biogeochemistry (BGC) and sediment (SED) modules w.r.t. (Tschumi et al., 2011).

module	parameter	new value	units	description
BGC	$\mathcal{R}_{\mathrm{Alk:P}}$	-17	–	Ratio Alk : P for photosynthesis/remineralisation
BGC	$\mathrm{Alk}_{\mathrm{init}}$	2429	$\mathrm{mol\,m^{-1}}$	initial Alk concentration
BGC	σ	0.68	–	DOM fraction of new production
BGC	$M_{\mathrm{CaCO_3}}$	0.25	–	maximum $CaCO_3$ production relative to POM
BGC	$l_{\mathrm{CaCO_3}}$	2900	m	$CaCO_3$ dissolution length-scale
BGC	α	0.83	–	exponent for Martin curve (POM remineralisation)
BGC	β	0.0018	–	Fe solubility
BGC	L_{tot}	1.2×10^{-6}	$\mathrm{mol\,m^{-1}}$	total ligand concentration
SED	$\mathcal{R}_{\mathrm{Alk:P}}$	-17	–	Redfield ratio Alk : P for organic matter
SED	F_{clay}	0.8	$\mathrm{g\,m^{-2}\,yr^{-1}}$	terrestrial clay flux
SED	r_{oxy}	100	$\mathrm{L\,mol^{-1}\,yr^{-1}}$	reactivity for POC/O_2
SED	r_{denit}	0	$\mathrm{L\,mol^{-1}\,yr^{-1}}$	reactivity for POC/NO_3 (denitrification)

Title Page
Abstract
Introduction
Conclusions
References
Tables
Figures
◀I
▶I
◀
▶
Back
Close
Full Screen / Esc
Printer-friendly Version
Interactive Discussion

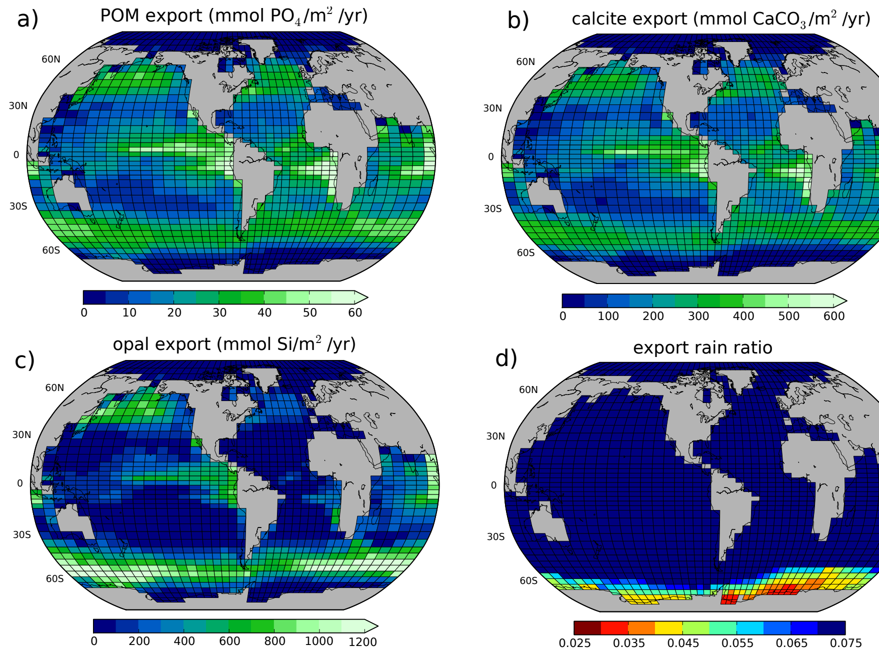

Fig. 1. Preindustrial, annual mean distribution of **(a)** POM export, **(b)** calcite export, **(c)** opal export. The ratio of inorganic to organic carbon export (rain ratio) is shown in **(d)**.

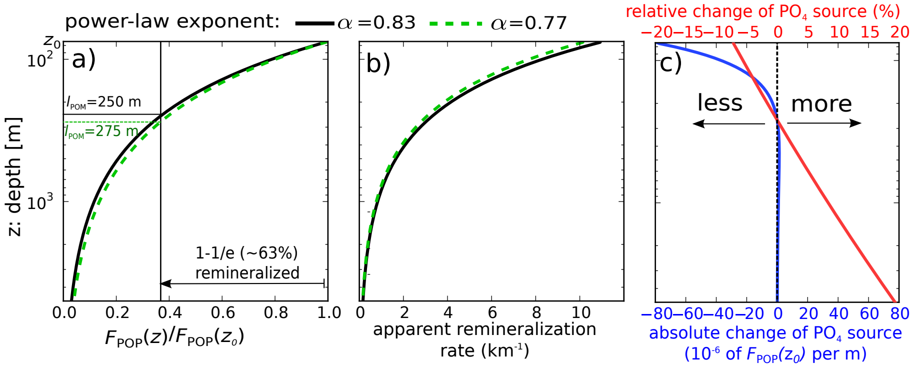

Fig. 2. (a) Parametrisation of the particulate organic matter flux within the water column (expressed here in terms of POP) out of the euphotic zone ($z_0 = 75\,\mathrm{m}$) according to a power-law $F(z) = F(z_0)\cdot(z/z_0)^{-\alpha}$ with $\alpha = 0.83$ being the base case (black line). The depth is positive downwards (note the logarithmic scaling). **(b)** The apparent rate of remineralisation (k/v), i.e. $-(\mathrm{d}F(z)/\mathrm{d}z)/F(z)$. The green line represents the corresponding values for a hypothetical deepening of the POM remineralisation ($\alpha = 0.83 \rightarrow 0.77$, or expressed as a change in the e-folding depth l_{POM}: 250 m → 275 m). Such a change leads to a decrease in upper ocean PO_4 source, while the deep ocean (below ~ 250 m) is enriched in PO_4 as depicted in **(c)**.

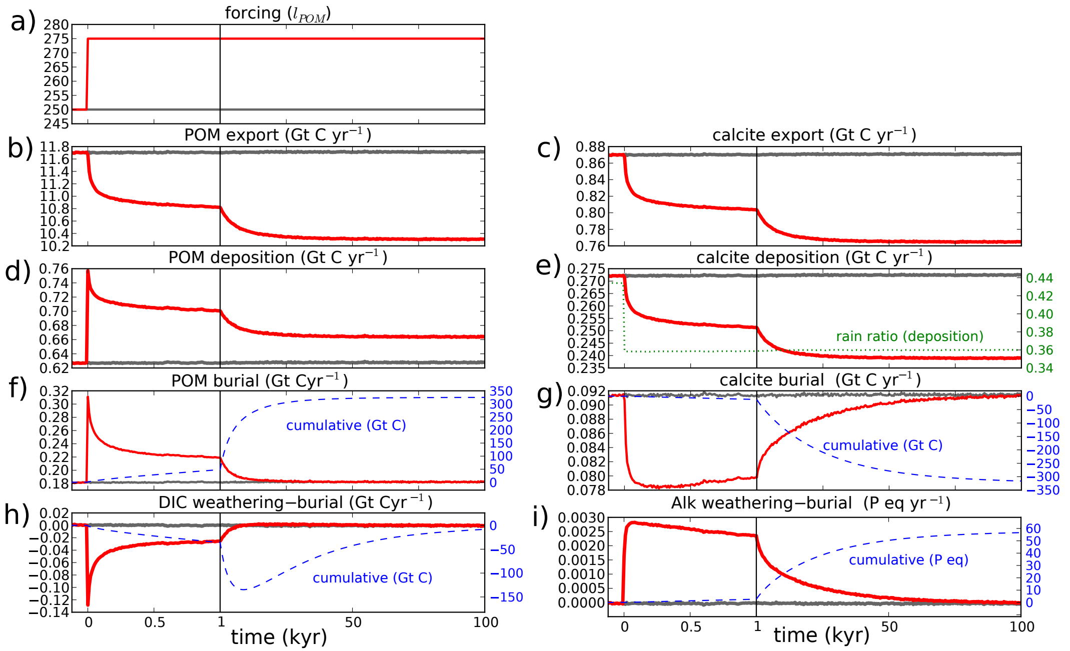

Fig. 3. Globally integrated, annual mean fluxes for the control run (grey, $l_{\text{POM}} = 250\,\text{m}$) and the perturbation experiment (red, $l_{\text{POM}} = 275\,\text{m}$). Note the different time axis for the first 1 kyr. Carbon *fluxes* are reported in gigatons of carbon (Gt C) and alkalinity fluxes in petaequivalents (P eq) (left *y* axis) per year. The blue dashed lines (right *y* axis) show *cumulative fluxes*, i.e. cumulative differences w.r.t. the control experiment. Weathering fluxes are kept constant in all experiments. The change in the ratio of the deposition flux of POC to $CaCO_3$ is shown by the green dotted line in **(e)**.

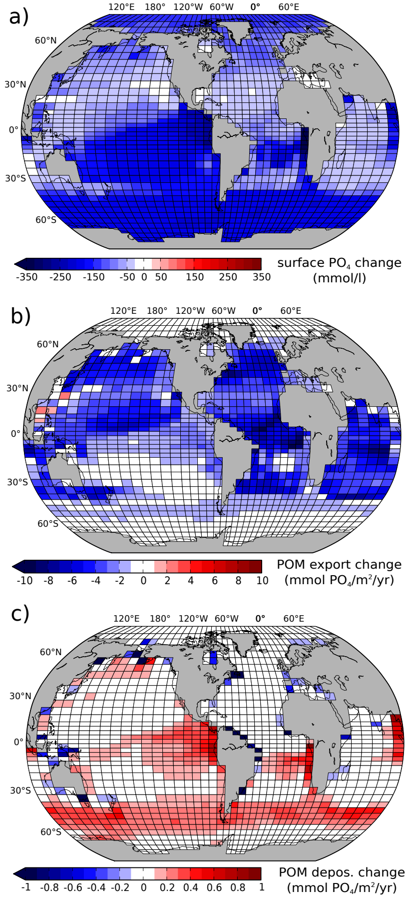

Fig. 4. Equilibrium changes in annual mean ocean properties in a POM remineralisation deepening experiment (l_{POM}: 250 m → 275 m). **(a)** Change in surface (top 80 m) seawater PO_4 concentration, **(b)** change in POM export flux and **(c)** change in seafloor POM deposition rate.

Title Page
Abstract Introduction
Conclusions References
Tables Figures
◀I ▶I
◀ ▶
Back Close
Full Screen / Esc
Printer-friendly Version
Interactive Discussion

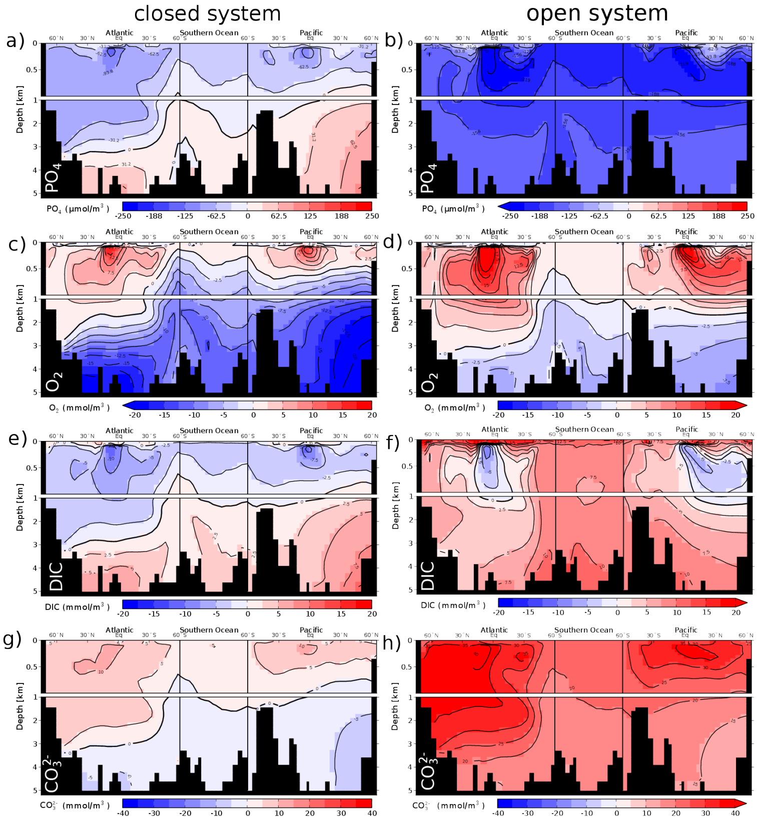

Fig. 5. Equilibrium changes in annual mean tracer concentrations in a POM deepening experiment (l_{POM}: 250 m → 275 m) with prognostic changes in export production along a transect through the Atlantic, Southern Ocean and Pacific (note that the top 1000 m are enlarged w.r.t. the deep ocean). Shown are (from top to bottom panels) changes in concentrations of phosphate, oxygen, dissolved inorganic carbon and carbonate. The experiments have been run both for the closed system (left column) as well as for the open system (right column).

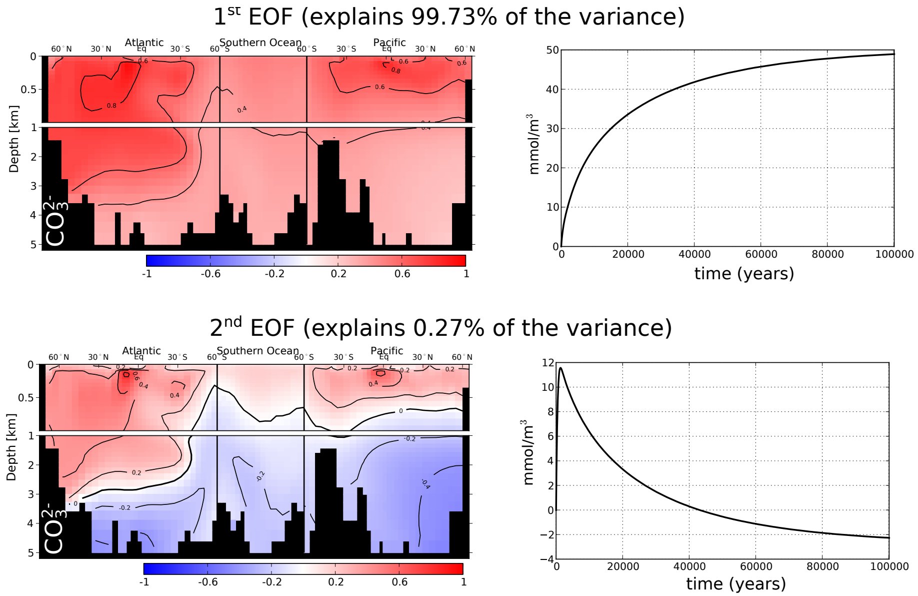

1st EOF (explains 99.73% of the variance)

2nd EOF (explains 0.27% of the variance)

Fig. 6. First two Empirical Orthogonal Functions (EOFs) (left panel) with corresponding Principal Components (timeseries; right panel) for the open-system response of CO_3^{2-}-anomalies in a POM deepening experiment (l_{POM}: 250 m → 275 m). The PC-EOF analysis was applied to the full 4-D tracer field; here the same section as in Fig. 5 is shown from the two EOFs.

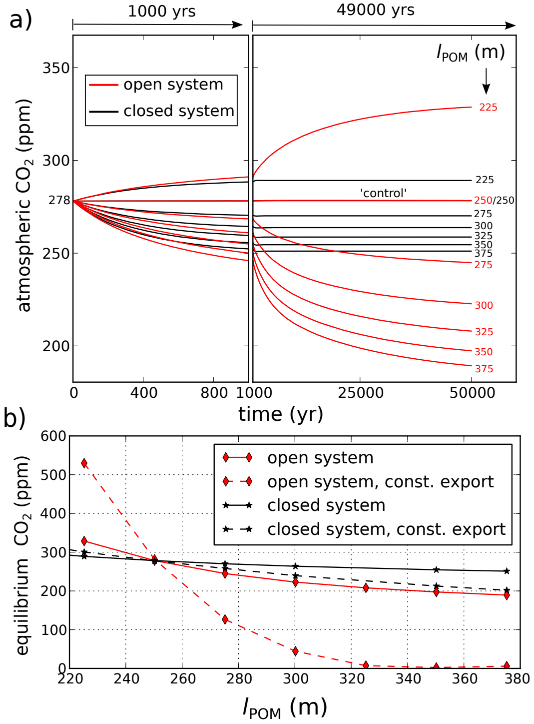

Fig. 7. (a) Time-evolution of atmospheric $p\mathrm{CO}_2$ as a result of instantaneous changes in the global POM remineralisation profiles for the open system (red) and the closed system (black). First 1000 yr of the time axis are enlarged. **(b)** $p\mathrm{CO}_2$ for a set of POM remineralisation depths with prognostic (solid lines) and constant (dashed lines) export production. Note that the constant export case does not equilibrate in the open system due to sustained weathering-burial imbalance. The corresponding values were calculated after 50 kyr.

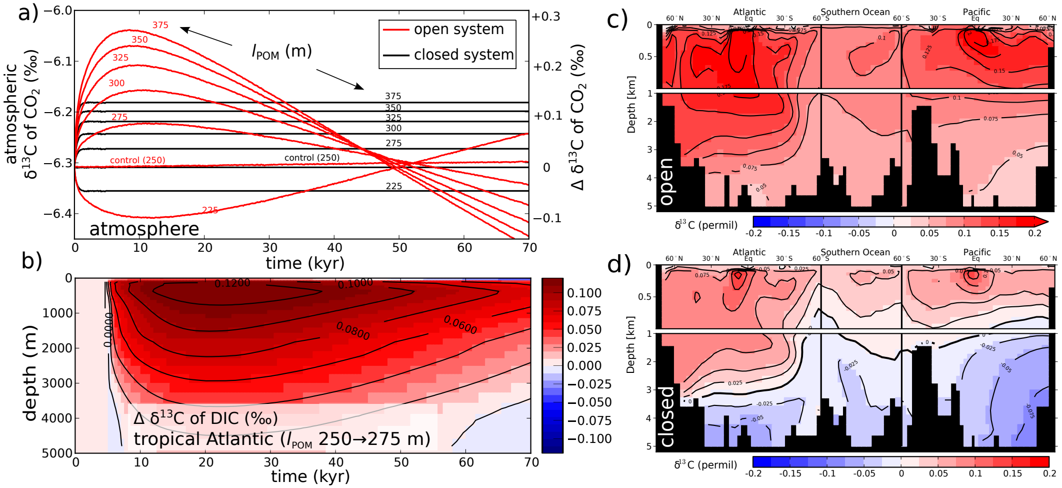

Fig. 8. **(a)** Time-evolution of the stable isotope $^{13}CO_2$ mixing ratio, expressed as $\delta^{13}C$ of CO_2, for a set of different POM remineralisation depths. The black line shows the response in the closed system, while the red lines show the evolution in the open system. **(b)** Hovmöller diagram of the change in $\delta^{13}C$ of DIC averaged over the tropical Atlantic. **(c, d)** Anomaly in $\delta^{13}C$ of DIC in the POM deepening experiment after 15 kyr in the open and closed system in a transect through the Atlantic, Southern Ocean and Pacific.

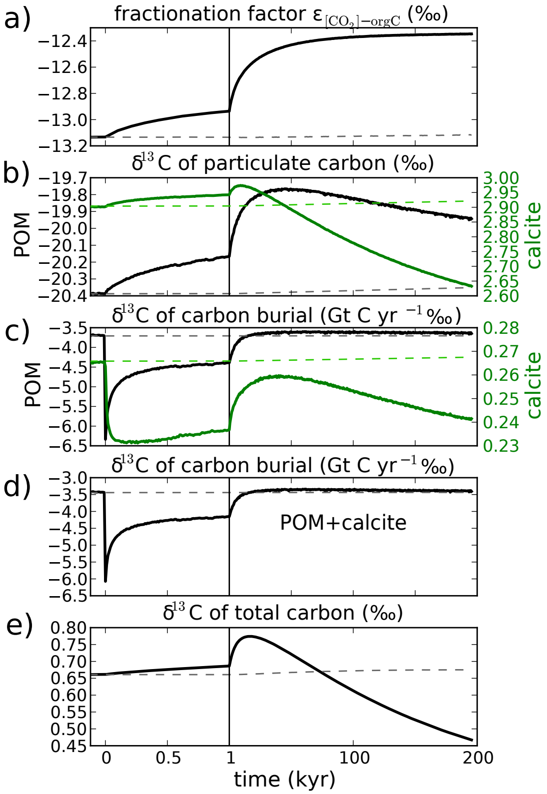

Fig. 9. Time-evolution of the oceanic ^{13}C-budget. **(a)** Fractionation during organic C formation (photosynthesis) expressed as $\epsilon = 1000 \cdot (\alpha - 1)$. **(b)** Isotopic signatures of particulate carbon in POM (black, left axis) and calcite (green, right axis). Burial of ^{13}C expressed as the C-burial flux times its isotopic signature in ‰ is shown in **(c)** for POM (black, left axis) and calcite (green, right axis) and for the total burial in **(d)**. **(e)** Average δ^{13}C signature of the carbon in the atmosphere–ocean system.

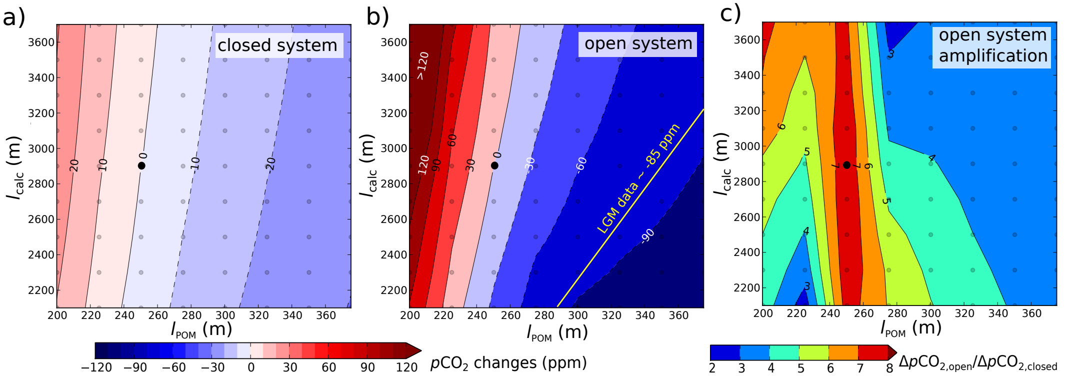

Fig. 10. Map of $\Delta p\text{CO}_2$ as a function of the length scale for the remineralisation of POM (l_{POM}) and of the length scale for the dissolution of CaCO_3 (l_{calc}). Values are differences with respect to the control-experiment with $l_{\text{POM}} = 250$ m and $l_{\text{calc}} = 2900$ m (black dots). Remineralisation/redissolution lengthscales changes are altered globally in these experiments. **(a)** is for a closed system, **(b)** for an open system, i.e. a setup allowing for weathering-burial dynamics. The LGM $p\text{CO}_2$ anomaly w.r.t. the Holocene (~ 85 ppm) is indicated by the yellow line. **(c)** shows the amplification of $p\text{CO}_2$ changes due to weathering-burial dynamics.

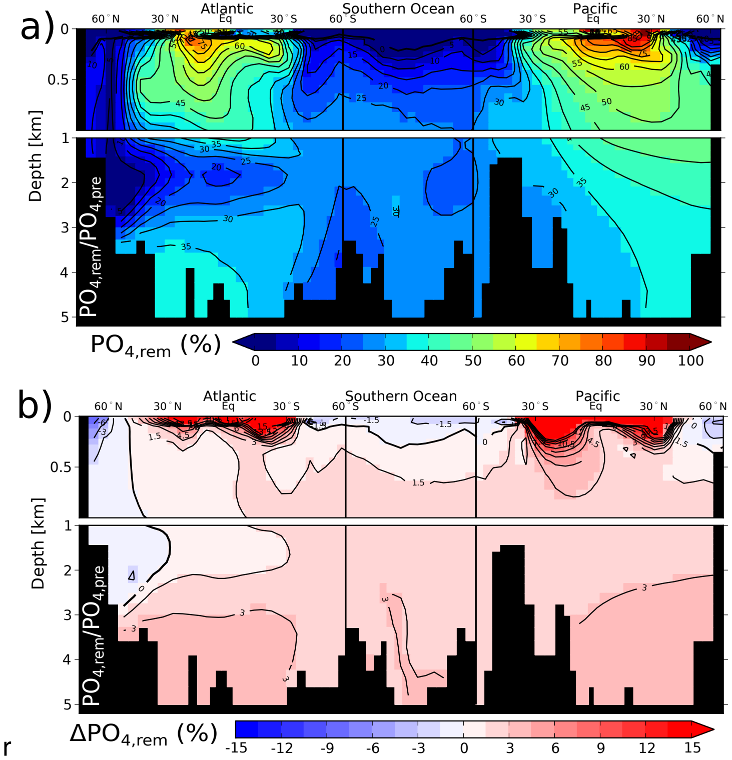

Fig. 11. (a) Percent fraction of remineralised : preformed nutrients in the control-simulation. Remineralised nutrient concentration is estimated as −AOU/170, where AOU denotes the apparent oxygen utilisation as calculated as $O_2 - O_{2,sat}$. **(b)** Change in this fraction in a POM deepening experiment (l_{POM}: 250 m → 275 m) in the open system.

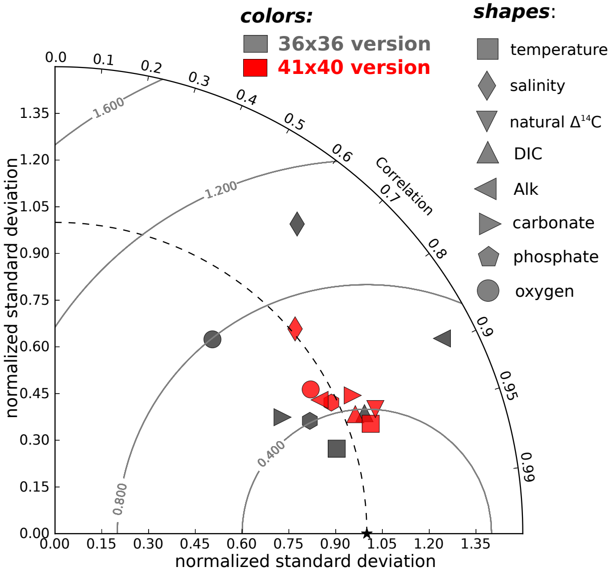

Fig. A1. Taylor diagram for global, volume-weighted oceanic tracer distributions. Results from the previous (36 × 36) model version are shown by grey and results from the updated version (41 × 40) by red symbols.

Title Page
Abstract
Introduction
Conclusions
References
Tables
Figures
◀I
▶I
◀
▶
Back
Close
Full Screen / Esc
Printer-friendly Version
Interactive Discussion

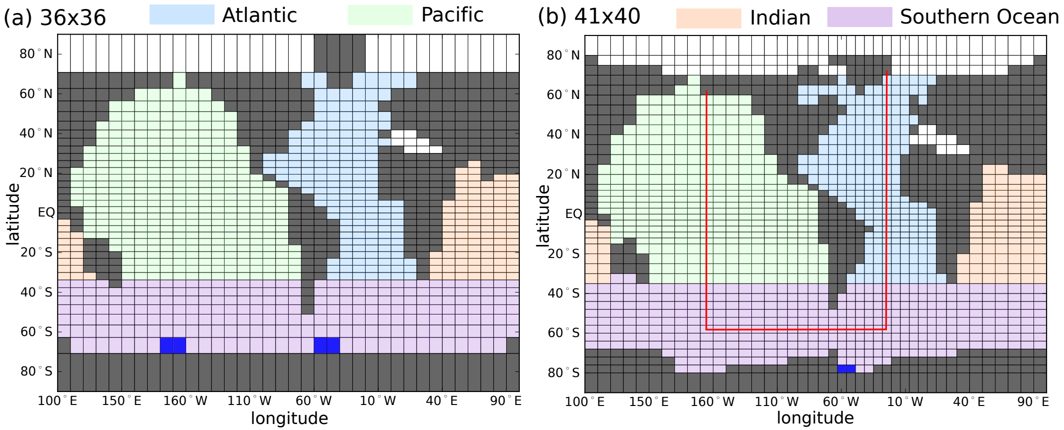

Fig. A2. Comparison of the horizontal grid for the previous (36 × 36) **(a)** and the updated (41 × 40) **(b)** version of the Bern3D ocean model. Both versions feature 32 depth layers. Latitudinal resolution near the equator remained largely unchanged while resolution was increased in the high-latitude. The ocean, atmosphere and sediment models share the same horizontal grid. The red line in **(b)** shows the path of the transect plot used in the main text. The blue colored cells indicate the locations of freshwater removal (i.e. the addition of salt) to stimulate deepwater formation. The light colors depict the definition of ocean basins as used to calculate depth gradients and zonal means.

Title Page
Abstract
Introduction
Conclusions
References
Tables
Figures
◀
▶
Back
Close
Full Screen / Esc
Printer-friendly Version
Interactive Discussion